

Extreme-value statistics of curl-of-vorticity precursor peaks in perturbed Taylor–Green vortex turbulence

Satori Tsuzuki¹

¹*Research Center for Advanced Science and Technology, The University of Tokyo*

(Dated: March 3, 2026)

Precursor peaks in the wavenumber $k_{\text{peak}}(t)$ maximizing the curl-of-vorticity spectrum have been observed to precede the dissipation peak in decaying turbulence. Because small perturbations in the initial condition can shift peak times, the associated lead time should be characterized statistically. We perform a pseudospectral DNS ensemble of $N_s = 1000$ perturbed Taylor–Green vortex realizations at $N = 256^3$ and $\nu = 10^{-3}$. For each run we extract $k_{\text{peak}}(t)$, several definitions of the precursor time t_k , the dissipation-peak time t_ε , and run-wise extrema including $K_{\text{max}} = \max_t k_{\text{peak}}(t)$ and $M_{\text{max}} = \max_t \max_k \mathcal{C}(k, t)$, where $\mathcal{C}(k, t)$ is the isotropic curl-of-vorticity spectrum. The distribution of $\Delta t_{\varepsilon, k} = t_\varepsilon - t_k$ shows that the precursor typically leads, while rare lagging realizations occur and are strongly conditioned on K_{max} . Using peaks-over-threshold extreme-value theory, we fit generalized Pareto models to the right tails of $X = -\Delta t_{\varepsilon, k}$ and M_{max} ; negative shape parameters indicate bounded tails and enable worst-case lag and endpoint estimates. Finally, M_{max} correlates strongly with ε_{max} and ensemble cross-correlations reveal a reproducible phase offset, supporting a dynamical coupling between high-curvature activity and dissipation bursts.

I. INTRODUCTION

Intermittent dissipation bursts are a defining feature of turbulence and motivate efforts to characterize not only their intensity but also their timing. In high-Reynolds-number flows, nonlinear advection transfers energy across a wide range of scales, intermittency emerges, and the dynamics often organizes into coherent vortical structures embedded in seemingly irregular motion. In the continuum regime, this evolution is governed by the deterministic incompressible Navier–Stokes equations; accordingly, a pseudospectral DNS produces a unique trajectory once the initial condition and physical parameters are specified. At the same time, turbulence is notoriously sensitive to small changes: tiny perturbations in the initial state or in modeling and discretization details can shift the occurrence times of extreme-gradient events, including the dissipation peak. Therefore, the timing of such events should be assessed statistically across an ensemble of perturbed realizations, and the practical performance of any precursor must be quantified in terms of reliability rather than by a single deterministic ordering. This viewpoint sets the stage for recent observations of spectral precursor peaks that tend to precede the dissipation maximum in decaying turbulence.

A recently identified precursor is based on the curl-of-vorticity spectrum. For the unperturbed Taylor–Green vortex (TGV), Tsuzuki [1] reported that the time at which the peak wavenumber $k_{\text{peak}}(t)$ attains its maximum precedes the time of maximum viscous dissipation. A subsequent study [2] showed that this ordering persists for moderate viscosities (e.g., $\nu = 10^{-3}$ or 2.5×10^{-4}) and several initial conditions, while it can be weakened or lost in highly viscous, diffusion-dominated cases (e.g., $\nu = 10^{-2}$). Note that, for the unperturbed TGV at $\nu = 2.5 \times 10^{-4}$, Ref. [2] used a companion 1024^3 simulation to avoid cutoff-proximate peak

locking in the k^4 -weighted (curl-of-vorticity) spectrum. These findings suggest that the precursor is robust yet problem-dependent. This motivates the central question addressed here: How reliable is the observed lead time under small but unavoidable perturbations?

The central goal of this paper is to quantify the uncertainty of the precursor timing in the canonical TGV when the initial condition is subjected to small random perturbations representing experimental or numerical uncertainties. We focus on two complementary aspects: (i) the *probabilistic reliability* of the precursor as measured by the distribution of $\Delta t_{\varepsilon, k} = t_\varepsilon - t_k$ and related conditional probabilities, and (ii) the *extreme-tail* behavior of large lags, modeled using peaks-over-threshold (POT) extreme-value theory. We translate a deterministic spectral precursor into a probabilistic reliability problem under unavoidable initial-condition uncertainty, and quantify worst-case failures via POT extreme-value theory.

Extreme-value theory background. Extreme-value theory (EVT) provides a probabilistic framework for modeling the tails of distributions and the statistics of unusually large (or small) observations. Let $\{X_i\}_{i=1}^n$ be independent and identically distributed (i.i.d.) random variables with cumulative distribution function (CDF) F , and let $Z_n = \max_{1 \leq i \leq n} X_i$ denote the sample maximum. The Fisher–Tippett–Gnedenko theorem states that if there exist normalizing constants $a_n > 0$ and b_n such that $(Z_n - b_n)/a_n$ converges in distribution to a nondegenerate limit, then that limit must belong to one of three types (Gumbel, Fréchet, or Weibull) and can be written in the unified generalized extreme-value (GEV) form [3, 4]

$$G(z; \mu, \sigma, \xi) = \exp \left\{ - \left[1 + \xi \frac{z - \mu}{\sigma} \right]^{-1/\xi} \right\},$$

$$1 + \xi \frac{z - \mu}{\sigma} > 0, \quad (1)$$

where $\mu \in \mathbb{R}$ is a location parameter, $\sigma > 0$ is a scale parameter, and ξ is the shape parameter (with the Gumbel case recovered as $\xi \rightarrow 0$). Distributions F for which such a limit exists are said to belong to the max-domain of attraction of a GEV law, and this condition underpins the block-maxima approach: one partitions a record into blocks, takes the maximum in each block, and fits a GEV model to the resulting sequence of block maxima.

A practical limitation of block maxima is that the number of maxima available for inference equals the number of blocks, which can be small when the record length is limited or when large blocks are required to justify approximate independence. To make more efficient use of tail information, EVT often adopts the peaks-over-threshold (POT) formulation, which models exceedances over a high threshold.

Peaks-over-threshold and generalized Pareto tails. In POT, one selects a high threshold u and considers the conditional excess distribution of $Y = X - u$ given $X > u$,

$$F_u(y) = \Pr(X - u \leq y \mid X > u) = \frac{F(u + y) - F(u)}{1 - F(u)}, \quad y \geq 0. \quad (2)$$

The Pickands–Balkema–de Haan theorem states that if F lies in a max-domain of attraction (the same broad condition that justifies GEV limits), then for sufficiently high u the excess distribution F_u is well approximated by a generalized Pareto distribution (GPD) [5, 6]

$$H(y; \xi, \beta) = \begin{cases} 1 - \left(1 + \xi \frac{y}{\beta}\right)^{-1/\xi}, & \xi \neq 0, \\ 1 - \exp\left(-\frac{y}{\beta}\right), & \xi = 0, \end{cases} \quad y \geq 0, \quad 1 + \xi \frac{y}{\beta} > 0, \quad (3)$$

where $\beta > 0$ is a scale parameter and ξ is the shape parameter. Importantly, ξ controls the tail type: $\xi > 0$ corresponds to heavy-tailed behavior, $\xi = 0$ to exponential-type tails, and $\xi < 0$ to bounded upper tails. In the bounded case $\xi < 0$, the fitted model implies a finite upper endpoint for X ,

$$x_{\text{end}} \equiv u - \frac{\beta}{\xi}, \quad (\xi < 0), \quad (4)$$

which is particularly useful when estimating worst-case scenarios (e.g., the largest plausible lag). More generally, POT enables estimation of high quantiles (return levels) using exceedance probabilities and the fitted GPD parameters.

In this work we apply POT to run-wise observables obtained from an ensemble of perturbed DNS realizations. Specifically, we analyze the right tails of $X = -\Delta t_{\varepsilon, k}$ (rare lagging cases) and of M_{max} , using high-quantile thresholds to maximize tail-information usage while retaining sufficient exceedances for stable inference (see Secs. II–III and Appendix D).

In related works, EVT and extreme/rare-event statistics have been increasingly used in fluid mechanics to connect intermittent bursts and regime changes to the tail behavior of physically meaningful observables. In transitional wall-bounded turbulence, Goldenfeld *et al.* linked the finite lifetime of turbulent transients to *extreme* fluctuations that drive decay, providing a statistical rationale for observed lifetime scalings [7]. Building on the idea that changes in stability should imprint themselves on extremes, Faranda *et al.* applied EVT-based diagnostics to detect global stability thresholds in transitional plane Couette flow [8]. In pipe flow, Nemoto and Alexakis directly examined whether large-amplitude bursts in turbulence intensity can trigger turbulent decay, quantifying how extreme events relate to decay-time statistics [9]; a broader perspective on how such extreme events manifest across transitional turbulence is summarized by Gomé *et al.* [10]. For fully developed Navier–Stokes turbulence, Yeung *et al.* characterized extreme events in DNS and their implications for small-scale intermittency [11], while Saw *et al.* provided an experimental characterization of extreme inertial-dissipation events in a turbulent swirling flow [12]. Focusing on tail statistics of small-scale gradients, Buaria *et al.* analyzed extreme velocity-gradient fluctuations [13] and later showed how the most intense events can self-attenuate through local dynamical mechanisms [14]. Complementing classical block-maxima or peak-over-threshold fitting, Farazmand and Sapsis introduced a variational strategy to probe and uncover dynamical precursors of extremes in turbulent systems [15], and Sapsis reviewed a wider toolbox for extreme-event statistics and prediction in fluid flows and waves [16].

While Refs. [1, 2] focused on the deterministic ordering and robustness of precursor peaks, the present work extends that framework to a perturbation ensemble and quantifies precursor reliability using extreme-value statistics. Building on the above studies, this study advances the field in three essential directions. First, rather than analyzing isolated extreme bursts or transition events, it formulates the *lead-lag relation* between a spectral precursor $k_{\text{peak}}(t)$ and the dissipation peak as a statistically well-defined random variable and quantifies it over a large DNS ensemble ($N_s = 1000$), thereby moving from deterministic observation to probabilistic characterization. Second, by applying a peaks-over-threshold extreme-value framework to the right tails of $X = -\Delta t_{\varepsilon, k}$ and of the run-wise maximum M_{max} , it provides bounded-tail estimates and principled worst-case lag bounds—an aspect that has not been explicitly quantified in prior turbulence-EVT studies. Third, the demonstrated strong correlation between M_{max} and ε_{max} , together with reproducible ensemble phase offsets, establishes a dynamical linkage between high-curvature spectral activity and dissipation bursts, thereby connecting statistical extreme-value structure to underlying Navier–Stokes dynamics. In this way, the study integrates precursor detection, ensemble uncertainty quantification, and EVT-based tail modeling into a unified

framework for assessing predictability and risk of extreme dissipation events in decaying turbulence.

The remainder of this paper is organized as follows. Section II describes the numerical methodology, ensemble construction, and definitions of the spectral observables and timing metrics. Section III outlines the peaks-over-threshold extreme-value framework and the associated inference procedure. Section IV presents the ensemble statistics and POT results. Section V discusses the physical interpretation, regime structure, and limitations of the analysis. Finally, Section VI summarizes the main findings and outlines directions for future work.

II. NUMERICAL METHOD AND DATASETS

Overview of DNS

We solve the incompressible Navier–Stokes equations in a periodic cube,

$$\partial_t \mathbf{u} + \mathbf{u} \cdot \nabla \mathbf{u} = -\nabla p + \nu \Delta \mathbf{u}, \quad (5)$$

$$\nabla \cdot \mathbf{u} = 0, \quad (6)$$

on $[0, 2\pi]^3$ using a Fourier pseudospectral method with the 2/3 de-aliasing rule. Time integration is performed with a classical four-stage fourth-order Runge–Kutta method (RK4) together with an integrating-factor treatment of the viscous term, as in Refs. [1, 2]. Unless stated otherwise, the reference ensemble uses $N = 256^3$ grid points, viscosity $\nu = 10^{-3}$, and a fixed time step $\Delta t = 10^{-3}$.

We store shell-averaged spectra at a cadence of 50 RK steps, corresponding to an output interval $\Delta t_{\text{out}} = 0.05$ in nondimensional units. All characteristic times reported below (e.g., t_k , t_ε , and t_M) are extracted from these discretely sampled outputs and are therefore quantized in steps of Δt_{out} . Conservatively, we assign an uncertainty $|\delta t| \leq \Delta t_{\text{out}}$ to each extracted event time, so that timing differences such as $\Delta t_{\varepsilon,k} \equiv t_\varepsilon - t_k$ have an uncertainty bounded by $|\delta \Delta t_{\varepsilon,k}| \leq 2\Delta t_{\text{out}}$. This choice follows Ref. [2], which used the same output interval under the same pseudo-spectral DNS protocol and showed that, in adequately resolved $\nu = 10^{-3}$ runs (passing spike inspection), the smallest separation between the peak-scale time and the dissipation-peak time was $|\Delta t_{\varepsilon,k}| = 0.40 \simeq 8 \Delta t_{\text{out}}$, well above the cadence-induced discretization bound. Using the same Δt_{out} here therefore enables direct comparison with Ref. [2] while providing adequate temporal resolution for the present parameter regime. Accordingly, when reporting lag-event probabilities we adopt a tolerance $\delta = 2\Delta t_{\text{out}}$ and classify a realization as a “lag event” only when $\Delta t_{\varepsilon,k} < -\delta$.

Initial condition perturbations

The baseline initial condition is the Taylor–Green vortex, originally introduced by Taylor and Green [17] and

widely used as a canonical decaying-turbulence configuration. Following the approach of Refs. [1, 2], we generate a family of perturbed initial conditions of the form

$$\mathbf{u}(\mathbf{x}, 0) = \mathbf{u}_{\text{TGV}}(\mathbf{x}) + w \mathbf{u}_{\text{rand}}(\mathbf{x}), \quad (7)$$

where $w = 0.05$ and \mathbf{u}_{rand} is a divergence-free random field whose Fourier support is limited to low wavenumbers ($k \leq 3$). For each seed, the perturbation phases are randomized and the full initial condition is rescaled such that the total kinetic energy is fixed at $E_0 = 0.125$. This construction isolates the effect of small-scale-agnostic initial uncertainty while keeping the gross energy level identical across the ensemble.

Spectral observables and timing definitions

We define vorticity $\boldsymbol{\omega} = \nabla \times \mathbf{u}$ and the curl of vorticity

$$\boldsymbol{\chi} \equiv \nabla \times \boldsymbol{\omega} = \nabla \times (\nabla \times \mathbf{u}) = -\Delta \mathbf{u}, \quad (8)$$

where the last identity uses incompressibility. Consequently, the shell-averaged spectrum of $|\boldsymbol{\chi}|^2$ is proportional to $k^4 E(k)$ for a solenoidal velocity field, and thus accentuates the development of small-scale content [2].

Let $\mathcal{C}(k, t)$ denote the isotropic (shell-averaged) spectrum of $|\boldsymbol{\chi}|^2$ at time t . We define the *peak wavenumber*

$$k_{\text{peak}}(t) \equiv \arg \max_k \mathcal{C}(k, t), \quad (9)$$

and its run-wise maximum

$$K_{\text{max}} \equiv \max_t k_{\text{peak}}(t). \quad (10)$$

The maximum amplitude of the curl-of-vorticity spectrum is

$$M(t) \equiv \max_k \mathcal{C}(k, t), \quad M_{\text{max}} \equiv \max_t M(t), \quad (11)$$

with peak time $t_M = \arg \max_t M(t)$.

We also compute the viscous dissipation rate $\varepsilon(t)$ (from the DNS outputs) and define the dissipation peak time

$$t_\varepsilon \equiv \arg \max_t \varepsilon(t), \quad \varepsilon_{\text{max}} \equiv \max_t \varepsilon(t). \quad (12)$$

To extract precursor timing, we use three operational definitions of the time t_k associated with the $k_{\text{peak}}(t)$ evolution:

- (i) *First hitting time* $t_{k,\text{first}}$: the earliest time at which $k_{\text{peak}}(t)$ reaches K_{max} .
- (ii) *Last hitting time* $t_{k,\text{last}}$: the latest time at which $k_{\text{peak}}(t)$ equals K_{max} .
- (iii) *Fractional time* $t_{k,s}$: the earliest time at which $k_{\text{peak}}(t) \geq s K_{\text{max}}$ for a prescribed fraction s ; in this work $s = 0.95$. We write $t_{k,95}$ to indicate the 95% level, using percentage notation for brevity.

TABLE I. DNS and dataset parameters for the main ensemble analyzed in this work.

| | |
|------------------------------|---|
| Domain | $[0, 2\pi]^3$ (periodic) |
| Grid | $N = 256^3$ |
| De-aliasing | 2/3 rule |
| Viscosity (reference) | $\nu = 10^{-3}$ |
| Time integration | RK4 with integrating factor (viscous term) |
| Time step | $\Delta t = 10^{-3}$ |
| Spectra sampling | every 50 steps ($\Delta t_{\text{out}} = 0.05$) |
| End time | $t_{\text{end}} = 20$ |
| Ensemble size | $N_s = 1000$ independent perturbation seeds |
| Initial total kinetic energy | $E_0 = 0.125$ |
| Perturbation weight | $w = 0.05$ (see Sec. II) |
| Perturbation bandwidth | $k \leq 3$ (low- k random field) |

The precursor lead/lag time is then

$$\Delta t_{\varepsilon,k} \equiv t_\varepsilon - t_k, \quad (13)$$

so that $\Delta t_{\varepsilon,k} > 0$ indicates a lead (precursor behavior) and $\Delta t_{\varepsilon,k} < 0$ indicates a lag. In addition, we define the time offset between the dissipation-peak time and the peak time of the maximum curl-of-vorticity amplitude, denoted by $\Delta t_{\varepsilon,M}$, as

$$\Delta t_{\varepsilon,M} \equiv t_\varepsilon - t_M. \quad (14)$$

We also define the ‘‘plateau duration’’ of the maximum-wavenumber state,

$$T_{\text{plat}} \equiv t_{k,\text{last}} - t_{k,\text{first}}, \quad (15)$$

which quantifies how long $k_{\text{peak}}(t) = K_{\text{max}}$ persists.

Spike inspection

Because $\mathcal{C}(k,t)$ emphasizes high wavenumbers, insufficient spatial resolution can cause spurious behavior in $k_{\text{peak}}(t)$, in particular a ‘‘cutoff-proximate peak locking’’ where $k_{\text{peak}}(t)$ sticks near the maximum resolved wavenumber. To prevent contamination of the precursor statistics by such numerical artifacts, we apply a spike inspection procedure. In brief, a run is flagged if $k_{\text{peak}}(t)$ resides within a prescribed fraction (here 95%) of the de-aliased isotropic cutoff wavenumber for any portion of the evolution, or if associated diagnostic conditions indicate a nonphysical high- k spike. All results reported for the reference case ($N = 256^3$, $\nu = 10^{-3}$) pass this inspection.

Spectral-resolution diagnostic. In addition to the spike inspection described above, we quantify the small-scale resolution by monitoring the standard pseudospectral indicator $k_{\text{max}}\eta(t)$. Here $\eta(t) = (\nu^3/\varepsilon(t))^{1/4}$ is the Kolmogorov length scale, and the dissipation rate is computed spectrally from the energy spectrum as $\varepsilon(t) = 2\nu \sum_k k^2 E(k,t)$. We report k_{max} at the Nyquist wavenumber ($k_{\text{max}} = N/2$) and also the effective maximum wavenumber after the 2/3 de-aliasing rule ($k_{\text{cut}} =$

$N/3$, so that $k_{\text{cut}}\eta = (2/3)k_{\text{max}}\eta$). For the resolved reference ensemble ($N = 256^3$, $\nu = 10^{-3}$, $N_s = 1000$), the minimum value over time, $\min_t(k_{\text{max}}\eta)$, is narrowly distributed across seeds: $2.165 \leq \min_t(k_{\text{max}}\eta) \leq 2.194$ (median 2.180, IQR [2.177, 2.183]). The corresponding de-aliased measure satisfies $1.443 \leq \min_t(k_{\text{cut}}\eta) \leq 1.463$ (median 1.453). Moreover, in every run the minimum $k_{\text{max}}\eta$ is attained at the dissipation-peak time $t_\varepsilon = \arg \max_t \varepsilon(t)$, i.e., $k_{\text{max}}\eta(t_\varepsilon) = \min_t(k_{\text{max}}\eta)$. A representative time series of $R_\lambda(t)$ and $k_{\text{max}}\eta(t)$ is provided in Appendix A (Fig. 6). Unless otherwise stated, all numerical diagnostics, including spike inspection, spectral normalization, shell averaging, and peak-time extraction, follow the conventions established in Ref. [2]. Table I summarizes the DNS setup and dataset parameters for the main ensemble analyzed in this work. The present study differs only in the ensemble construction and the subsequent extreme-value analysis.

III. EXTREME-VALUE STATISTICS METHOD

The objective of the present analysis is to quantify not only the typical precursor lead time but also rare realizations in which the precursor fails, i.e., exhibits a substantial lag relative to the dissipation peak. To this end, we model the upper tail of a scalar run-wise quantity X using the peaks-over-threshold (POT) framework. In the present context, X is primarily taken to be the lag magnitude

$$X = -\Delta t_{\varepsilon,k}, \quad (16)$$

so that large values of X correspond to strong lagging cases. We also apply POT to M_{max} in order to characterize the extreme amplitude of the curvature proxy.

Run-wise sampling and independence

Each realization in our ensemble corresponds to a distinct randomly perturbed initial condition. For a fixed seed, the DNS evolution is deterministic; however, across

seeds the extracted run-wise observables (e.g., $\Delta t_{\varepsilon,k}$ and M_{\max}) form a collection of independent samples under the assumption that the perturbations are independently drawn. Thus, for the purpose of extreme-value modeling, we treat

$$X_1, \dots, X_{N_s} \quad (17)$$

as approximately independent and identically distributed (i.i.d.) samples from an underlying distribution F . Importantly, we apply extreme-value theory to one scalar value per run, rather than to strongly correlated time-series data, which substantially mitigates concerns about temporal dependence.

Peaks-over-threshold formulation

Given i.i.d. samples X_1, \dots, X_n with cumulative distribution function F , the conditional excess distribution above a high threshold u is defined as

$$F_u(y) \equiv \mathbb{P}(X - u \leq y \mid X > u), \quad y \geq 0. \quad (18)$$

The Pickands–Balkema–de Haan theorem (see Appendix C) states that if F lies in a suitable max-domain of attraction, then for sufficiently high u the excess distribution F_u is well approximated by a generalized Pareto distribution (GPD).

The GPD is given by

$$H(y; \xi, \beta) = \begin{cases} 1 - \left(1 + \xi \frac{y}{\beta}\right)^{-1/\xi}, & \xi \neq 0, \\ 1 - \exp\left(-\frac{y}{\beta}\right), & \xi = 0, \end{cases} \quad (19)$$

$$y \geq 0, \quad 1 + \xi \frac{y}{\beta} > 0,$$

where ξ is the shape parameter and $\beta > 0$ is the scale parameter. Note that Eq. (19) is a restatement of Eq. (3). The sign of ξ determines the tail class: $\xi > 0$ corresponds to heavy-tailed behavior, $\xi = 0$ to exponential-type decay, and $\xi < 0$ to a bounded upper tail. In the latter case, the fitted model implies a finite upper endpoint

$$x_{\text{end}} \equiv u - \frac{\beta}{\xi}, \quad (\xi < 0), \quad (20)$$

which provides an estimate of the largest plausible extreme event under the model.

Threshold choice and inference

In practice, we select a high empirical quantile threshold u , taken here as the $q = 0.9$ quantile of the sample unless otherwise noted. This choice represents a compromise: the threshold must be high enough for the GPD approximation to be valid, yet low enough to retain a

sufficient number of exceedances for stable parameter estimation. For $N_s = 1000$ and a $q = 0.9$ threshold, this typically yields $\mathcal{O}(10^2)$ exceedances (here $n_u \approx 86$ –100 depending on ties; see Table II).

We fit the GPD parameters (ξ, β) to the exceedances

$$Y_i = X_i - u, \quad X_i > u, \quad (21)$$

by maximum likelihood, fixing the GPD location parameter at zero. We report the fitted threshold u , the estimated shape and scale parameters, and, when $\xi < 0$, the implied upper endpoint. Sensitivity to the threshold is examined by varying q in a moderate range and confirming qualitative robustness of the inferred tail class.

IV. RESULTS

We first analyze the statistically resolved reference ensemble consisting of $N_s = 1000$ perturbed realizations at $N = 256^3$ and $\nu = 10^{-3}$. All runs pass the spike inspection and satisfy the resolution diagnostic discussed in Appendix A, ensuring that the spectral peak statistics are not contaminated by cutoff locking.

A. Representative realizations and precursor definitions

Figure 1 shows representative time series of $k_{\text{peak}}(t)$ and $\varepsilon(t)$, together with the timing markers $t_{k,\text{first}}$, $t_{k,95}$, $t_{k,\text{last}}$, and t_ε . The panels illustrate that (i) $k_{\text{peak}}(t)$ typically increases as the cascade populates higher wavenumbers, (ii) the maximum K_{\max} is often attained over a finite plateau, and (iii) the ordering between t_k and t_ε depends on which operational definition of t_k is adopted. In particular, $t_{k,\text{first}}$ and $t_{k,95}$ are designed to emphasize the onset of the plateau and thus act as precursors, whereas $t_{k,\text{last}}$ can occur after t_ε and is therefore not intended as a leading indicator.

B. Distribution of K_{\max} and conditional lag probability

Figure 2 summarizes the ensemble variability of K_{\max} and the conditional probability of “lag events” $\Delta t_{\varepsilon,k} < -0.1$ given K_{\max} . For the present ensemble ($N_s = 1000$), K_{\max} takes a small set of discrete values (31, 33, 34, 36), with the majority at $K_{\max} = 34$. Quantitatively, the observed K_{\max} counts are as follows:

| K_{\max} | count | fraction |
|------------|-------|----------|
| 31 | 4 | 0.004 |
| 33 | 38 | 0.038 |
| 34 | 875 | 0.875 |
| 36 | 83 | 0.083 |

Two trends are apparent in Fig. 2(a): (i) most realizations fall into $K_{\max} = 34$, where the lag probability is modest and can be strongly reduced by adopting the fractional definition $t_{k,95}$ instead of $t_{k,\text{first}}$; and (ii) realizations with $K_{\max} = 36$ are substantially more likely to exhibit lag, suggesting that the large- K_{\max} branch corresponds to a distinct dynamical pathway (or to a different discretization regime of the spectral-peak trajectory; see Appendix B).

C. Ensemble distributions of precursor lead time and plateau duration

Figure 3(a) shows the empirical cumulative distribution functions (ECDFs) of $\Delta t_{\varepsilon,k}$ for three t_k definitions. The distributions for $t_{k,\text{first}}$ and $t_{k,95}$ are centered on positive values (typical lead), but they exhibit a negative tail corresponding to occasional lagging cases. By contrast, the distribution for $t_{k,\text{last}}$ is shifted to negative values, reflecting that the maximum-wavenumber plateau can persist beyond the dissipation peak. Figure 3(b) shows the ECDF of the plateau duration T_{plat} , which has broad support up to ≈ 5.5 (nondimensional time units), indicating that $k_{\text{peak}}(t) = K_{\max}$ often persists over an extended interval rather than at an isolated instant. Finally, Fig. 3(c) shows that M_{\max} and ε_{\max} are strongly correlated across realizations (Pearson correlation ≈ 0.819), implying that runs with stronger high-curvature activity also tend to realize stronger dissipation bursts.

D. POT modeling of extreme lags and extreme

M_{\max}

We now quantify the most extreme lag events using POT EVT. For each timing definition, we consider the transformed variable $X = -\Delta t_{\varepsilon,k}$ and focus on its upper tail. Figure 4 shows the empirical survival function $\Pr(X > x)$ and the fitted GPD tail overlay. In all cases the fitted shape parameter is negative ($\hat{\xi} < 0$), implying a bounded upper tail and enabling an estimate of the worst-case lag magnitude at this resolution. We also apply POT to M_{\max} and likewise obtain $\hat{\xi} < 0$. This should be interpreted as an *effective* bound for the sampled distribution under the present resolution and ensemble, rather than as a strict mathematical bound for the continuum dynamics. For transparency and reuse, Table II summarizes the fitted POT parameters using a common quantile threshold $q = 0.9$. To assess threshold sensitivity and parameter uncertainty, we additionally performed fixed-threshold bootstrap resampling for each POT fit. Table III reports 95% confidence intervals for $(\xi, \beta, x_{\text{end}})$, and Figs. 7–9 provide complementary diagnostics (exceedance–threshold tradeoff, bootstrap histograms, and mean residual life plots).

E. Time-resolved relationship between $M(t)$ and $\varepsilon(t)$

Figure 5 reports an auxiliary analysis based on time series written at the spectral sampling cadence. We compute the ensemble cross-correlation $\text{corr}[M(t), \varepsilon(t + \tau)]$ and identify the lag τ^* that maximizes this correlation for each realization. Across all realizations, τ^* is narrowly distributed around ≈ -0.85 , implying that $\varepsilon(t)$ tends to lead $M(t)$ by about 0.85. Importantly, this ordering concerns the *amplitude* $M(t)$, whereas the precursor studied in Figs. 1–4 concerns the *wavenumber location* $k_{\text{peak}}(t)$. The two diagnostics therefore capture different aspects of the approach to the dissipation peak: scale localization (shift of k_{peak}) versus intensity growth (rise of M).

F. Unresolved low-viscosity case (spike-flagged)

To clarify the limits of the precursor analysis, we also performed simulations at a lower viscosity $\nu = 2.5 \times 10^{-4}$. At $N = 256^3$, all realizations are flagged by spike inspection: the peak wavenumber locks at the de-aliased isotropic cutoff ($K_{\max} = 86$ for this configuration), indicating insufficient resolution for reliable statistics of the curl-of-vorticity spectrum. A smaller set of $N = 512^3$ runs (not analyzed statistically here) exhibits the same failure mode, suggesting that substantially higher resolution would be required for this viscosity. We therefore treat the low-viscosity dataset as a diagnostic cautionary example rather than as a target for EVT modeling.

V. DISCUSSION

The DNS dynamics and the spectral post-processing are deterministic once the initial condition is fixed. Nevertheless, for both experiments and computations, one rarely has access to the exact “true” initial condition: small perturbations (measurement noise, unmodeled background fluctuations, discretization and calibration uncertainty) imply that the precursor outcomes should be treated as *random variables* sampled from an ensemble. From the perspective of statistical physics, the present study therefore asks a concrete question: *given a well-defined perturbation ensemble around a canonical turbulent flow (TGV), what can extreme-value statistics say about the reliability and the worst-case behavior of a spectral precursor?*

A. From a deterministic precursor to probabilistic reliability

For a single realization, the ordering $t_k < t_\varepsilon$ is a statement about a particular trajectory. Across the ensemble, the relevant objects are the distributions of (i) the scale indicator $k_{\text{peak}}(t)$ and its hitting times $t_{k,\text{first}}$, $t_{k,95}$,

TABLE II. The fitted POT parameters using a common quantile threshold $q = 0.9$

| Variable | n | q | u | p_u | $\hat{\xi}$ | $\hat{\beta}$ | \hat{x}_{end} |
|--|------|------|------|-------|-------------|---------------|------------------------|
| $-\Delta t_{\varepsilon,k}^{(\text{first})}$ | 1000 | 0.90 | 0.25 | 0.093 | -0.228 | 0.421 | 2.10 |
| $-\Delta t_{\varepsilon,k}^{(s=0.95)}$ | 1000 | 0.90 | 0.00 | 0.086 | -0.239 | 0.431 | 1.80 |
| $-\Delta t_{\varepsilon,k}^{(\text{last})}$ | 1000 | 0.90 | 1.35 | 0.099 | -0.226 | 0.310 | 2.72 |
| M_{max} | 1000 | 0.90 | 76.0 | 0.100 | -0.256 | 0.953 | 79.8 |

and $t_{k,\text{last}}$, (ii) the lag variables $\Delta t_{\varepsilon,k} = t_{\varepsilon} - t_k$ under these definitions, and (iii) run-wise intensity measures such as M_{max} and ε_{max} . Figure 1 illustrates why these objects are not redundant: the *scale* at which the curl-of-vorticity spectrum concentrates (tracked by k_{peak}) can evolve in a step-like fashion and produce multiple plausible “event times” even when $\varepsilon(t)$ remains smooth. In this setting, “precursor reliability” can be expressed in an operational form, e.g. as $\mathbb{P}(\Delta t_{\varepsilon,k} < -\delta)$ for a tolerance δ representing the minimal lead time that can be resolved or exploited. The conditional probabilities in Fig. 2(a) show that this reliability is not a single number: it is strongly *state dependent*.

B. A discrete state variable: why conditioning on K_{max} is informative

A salient empirical feature is that $K_{\text{max}} = \max_t k_{\text{peak}}(t)$ takes only a small number of discrete values at the present resolution. For the $N_s = 1000$ reference ensemble, the distribution is dominated by $K_{\text{max}} = 34$ (875 runs, 87.5%), with secondary branches at $K_{\text{max}} = 36$ (83 runs, 8.3%), $K_{\text{max}} = 33$ (38 runs, 3.8%), and a very small remainder at $K_{\text{max}} = 31$ (4 runs); see Fig. 2(b). This discreteness is not a drawback; it is a *diagnostic*: it partitions the ensemble into distinct regimes with markedly different failure rates. In particular, Fig. 2(a) shows that the lag probability $\mathbb{P}(\Delta t_{\varepsilon,k} < -0.1)$ is smallest in the dominant $K_{\text{max}} = 34$ regime, while it is substantially elevated in the $K_{\text{max}} = 36$ branch and is also non-negligible in the $K_{\text{max}} = 33$ branch. This structure is difficult to infer from unconditional summary statistics alone. From a modeling viewpoint, the results therefore favor a *mixture* (or stratified) interpretation: the ensemble is better described as a superposition of sub-populations indexed by a discrete spectral state variable K_{max} . A practical implication follows. If a measurement protocol (or online diagnostic) can determine whether a realization is evolving toward a higher- K_{max} branch, then the inferred “risk” of precursor failure can be updated in a regime-aware manner. In this sense, K_{max} acts as a compact “state label” that carries predictive information beyond the instantaneous lead time itself.

C. Robust timing definitions and the role of the k_{peak} plateau

The ECDFs in Fig. 3(a) confirm that the choice of t_k definition matters. The last-hitting time $t_{k,\text{last}}$ produces systematically smaller $\Delta t_{\varepsilon,k}$ (i.e. later inferred precursor times), consistent with the plateau interpretation: once $k_{\text{peak}}(t)$ reaches K_{max} , it can remain there for a finite span, and the *duration* of this plateau controls how far $t_{k,\text{last}}$ can be delayed relative to $t_{k,\text{first}}$. Figure 3(b) quantifies this reoccurrence span and shows that plateau durations are broadly distributed and can extend over several turnover-time fractions. In this light, $t_{k,95}$ can be viewed as a compromise between early sensitivity and late-time ambiguity. Operationally, it corresponds to the first time that the scale indicator enters a high- k band close to K_{max} , suppressing spurious early steps while remaining insensitive to long plateaus. The reduction of the conditional lag probability in the dominant $K_{\text{max}} = 34$ regime (Fig. 2(a)) provides an empirical validation of this robustness criterion.

D. Extreme-event viewpoint: bounded tails, uncertainty, and threshold diagnostics

A main contribution of extreme-value theory (EVT) in the present context is that it targets the rare events that most directly affect *risk*: large negative $\Delta t_{\varepsilon,k}$ (i.e. cases where the precursor time trails the dissipation peak by an amount that would compromise predictability). We therefore modeled the tail of $X = -\Delta t_{\varepsilon,k}$ using the POT framework (Fig. 4). With $N_s = 1000$, the inference of *bounded* tails is substantially more robust than in the smaller ensemble: (i) the POT fits yield $\hat{\xi} < 0$ for all four variables considered, and (ii) bootstrap confidence intervals for ξ are strictly negative, with a bootstrap frequency of $\hat{\xi} \geq 0$ below 0.2 % for any variable (Table III). This supports the interpretation that, under the present measurement protocol and within the resolved reference regime, the right tails of $X = -\Delta t_{\varepsilon,k}$ and M_{max} are effectively Weibull-type. At the same time, EVT diagnostics clarify an important trade-off. Increasing the threshold u reduces the number of exceedances n_u and thus increases parametric uncertainty; Fig. 7 makes this trade-off explicit for all four variables.

Moreover, the mean residual life (MRL) curves (Fig. 9) are broadly consistent with a decreasing, approximately

linear trend at intermediate thresholds (as expected for $\xi < 0$), but become progressively noisier as u increases and n_u shrinks. These observations motivate a “goldilocks” threshold selection: high enough for the GPD approximation to be credible, but not so high that the fit becomes dominated by a handful of points. Finally, bootstrap histograms (Figs. 7–8) highlight that endpoint estimates can be sensitive to finite-sample variability, especially when $\hat{\xi}$ is close to zero (even if negative). For the present dataset, the fitted endpoints and their confidence intervals should therefore be interpreted as *protocol- and sample-dependent worst-case bounds* rather than as strict continuum invariants. The key point is not that the endpoint is known with high precision, but that bounded-tail behavior is consistently supported and that the implied worst-case lag magnitudes remain $\mathcal{O}(1)$ in the nondimensional time units used here.

E. Physical meaning of curl-of-vorticity spectral intensity: coupling to dissipation and phase relations

Beyond timing, the ensemble reveals a tight relationship between curl-of-vorticity activity and dissipation intensity: Fig. 3(c) shows a strong positive correlation between M_{\max} and ε_{\max} (Pearson $r \approx 0.819$ for $N_s = 1000$). Here $M(t)$ (and hence M_{\max}) is defined as the maximum over wavenumber of the curl-of-vorticity spectrum, i.e. $M(t) = \max_k \mathcal{C}(k, t)$, so it preferentially weights the smallest dynamically active scales captured by the spectrum. The observed correlation therefore supports the interpretation that realizations with stronger high-curvature spectral activity also tend to realize stronger dissipation bursts, reinforcing the physical relevance of curl-of-vorticity diagnostics.

At the same time, the time-resolved cross-correlation analysis (Fig. 5) clarifies that “physical relevance” does not automatically imply “causal precedence” in time. Both the peak-time offset $\Delta t_{\varepsilon, M} = t_\varepsilon - t_M$ and the optimal-lag statistics $\tau^* = \arg \max_\tau \text{corr}[M(t), \varepsilon(t + \tau)]$ indicate that $M(t)$ typically peaks *after* $\varepsilon(t)$ by a fraction of a unit time. This is consistent with a picture in which the dissipation peak marks the culmination of energy removal, while the most intense higher-derivative spectral curvature measure continues to sharpen slightly later as the cascade reorganizes small-scale structures. Importantly, this behavior can coexist with the precursor property of $k_{\text{peak}}(t)$: the *dominant scale* of curl-of-vorticity activity can reach near-saturation (affecting t_k) before the *amplitude* $M(t)$ attains its maximum.

F. Limitations, resolution requirements, and outlook

Finally, the low-viscosity case highlights a key methodological point: EVT cannot rescue under-resolved di-

agnostics. Spike inspection is essential when analyzing high- k -sensitive indicators; otherwise, cutoff-proximate locking can masquerade as extreme precursor behavior. In the present work, this inspection justifies restricting EVT-based conclusions to the resolved reference case. For completeness, we also report the time evolution of the classical resolution indicator $k_{\max}\eta$ (Appendix A), which remains safely above unity at Nyquist for the reference dataset.

Several extensions are natural. On the physics side, it is important to test whether the mixture structure in K_{\max} persists at higher resolution and across different perturbation amplitudes and initial-condition families. On the statistics side, the POT fits and their diagnostics (Appendix D) can be extended to systematic threshold-selection criteria and to joint/conditional tail models (e.g. conditioning on K_{\max} or coupling M_{\max} and ε_{\max} in a multivariate EVT framework). More broadly, the methodology here provides a template for translating deterministic “precursor” observations into quantitative uncertainty bounds, which is a prerequisite for assessing observability and practical predictability in laboratory measurements and numerical models.

VI. CONCLUSIONS

We investigated the statistical robustness of a turbulence precursor based on the *curl-of-vorticity* spectrum in perturbed Taylor–Green vortex (TGV) turbulence. Although the underlying pseudospectral DNS is deterministic, the precursor timing becomes practically uncertain once one accounts for small perturbations to the initial condition (representing experimental uncertainty, numerical uncertainty, or uncontrolled fluctuations). To quantify this uncertainty, we performed an ensemble of $N_s = 1000$ perturbed TGV realizations at $N = 256^3$ and $\nu = 10^{-3}$ and analyzed ensemble-level fluctuations using peaks-over-threshold (POT) extreme-value statistics.

What we learned. Our main findings can be summarized as follows:

- 1. Ensemble variability of precursor timing is measurable and highly structured.** The lead time $\Delta t_{\varepsilon, k} = t_\varepsilon - t_k$ is broadly positive for the resolved reference case, but a statistically significant negative tail exists (rare “precursor failures” with $t_k > t_\varepsilon$). Moreover, the failure probability is strongly conditioned on the discrete wavenumber maximum $K_{\max} = \max_t k_{\text{peak}}(t)$. For $N_s = 1000$, the ensemble is dominated by $K_{\max} = 34$ (875 runs), with secondary branches at $K_{\max} = 36$ (83 runs) and $K_{\max} = 33$ (38 runs) (Fig. 2). The conditional lag probability $\mathbb{P}(\Delta t_{\varepsilon, k} < -0.1)$ is smallest in the $K_{\max} = 34$ regime and is substantially larger in the higher- K_{\max} branch, demonstrating that precursor reliability is state dependent rather than universal.
- 2. A more robust t_k definition can be justified**

and validated statistically. Defining t_k via the fractional criterion $t_{k,s}$ (here $s = 0.95$) reduces the incidence of lagging events in the dominant $K_{\max} = 34$ group while largely preserving the typical leading behavior (Fig. 2). This provides a concrete, data-driven route to *redefining* the precursor time so as to mitigate ambiguity caused by the finite plateau of $k_{\text{peak}}(t)$ at K_{\max} .

3. **The severity of rare lagging events admits EVT-based upper bounds, with quantified uncertainty.** Applying POT to the lag magnitude $X = -\Delta t_{\varepsilon,k}$ yields negative GPD shape parameters for all three t_k definitions, implying bounded right tails in the present ensemble. Using a fixed $q = 0.9$ threshold and bootstrap resampling, we find strictly negative 95% confidence intervals for ξ for all variables, and a bootstrap frequency of $\hat{\xi} \geq 0$ below 0.2 % in all cases (Table III). Endpoint estimates are finite but have non-negligible uncertainty, reflecting the expected exceedance/variance trade-off at high thresholds (Appendix D); nevertheless, the fitted endpoints remain $\mathcal{O}(1)$ for $X = -\Delta t_{\varepsilon,k}$ in the present nondimensional units.
4. **The curl-of-vorticity spectral intensity is dynamically linked to dissipation bursts.** Across realizations, the run-wise curl-of-vorticity spectral intensity $M_{\max} = \max_t \max_k C(k, t)$ correlates strongly with the dissipation peak ε_{\max} (Pearson $r \approx 0.82$), indicating that high-curvature spectral activity co-varies with an energetically meaningful quantity. Time-resolved analysis further shows a reproducible phase offset between $M(t)$ and $\varepsilon(t)$ (Fig. 5), with $M(t)$ typically peaking after $\varepsilon(t)$, while the *wavenumber localization* signal $k_{\text{peak}}(t)$ remains a viable precursor in many realizations.
5. **Resolution screening is essential for preventing spurious EVT conclusions in under-resolved cases.** For the lower-viscosity case $\nu = 2.5 \times 10^{-4}$, spike inspection flags cutoff-proximate peak locking at both $N = 256^3$ and $N = 512^3$, indicating that the spectra are not adequately resolved for reliable precursor/EVT inference. This motivates a resolution-first workflow: only ensembles passing spike inspection (and classical criteria such as $k_{\max}\eta$) should be subjected to tail modeling.

Outlook. The present study opens several concrete directions. First, extending the ensemble to lower viscosities will require systematically increasing resolution (and possibly refining dealiasing/cutoff choices) to avoid peak locking. Second, the observed conditioning on K_{\max} motivates stratified (or hierarchical) EVT models that explicitly incorporate discrete spectral states. Third, the strong $M_{\max}-\varepsilon_{\max}$ correlation and the reproducible phase relation between $M(t)$ and $\varepsilon(t)$ point to a dynamical mechanism linking high-curvature activity to dissipation events; establishing this mechanism will likely require

joint real spectral-space diagnostics (e.g. structure geometry, enstrophy production, and local strain–vorticity alignment) and, potentially, multivariate or conditional EVT approaches. Finally, the methodology here provides a template for translating deterministic “precursor” observations into quantitative uncertainty bounds, which is a prerequisite for assessing observability and practical predictability in laboratory measurements and numerical models.

ACKNOWLEDGMENTS

This study was supported by JSPS KAKENHI (Grant Number 22K14177) and JST PRESTO (Grant Number JPMJPR23O7).

Appendix A: Resolution diagnostic based on $k_{\max}\eta$

To complement the spike inspection, we report the temporal evolution of the Taylor-microscale Reynolds number $R_\lambda(t)$ together with the resolution indicator $k_{\max}\eta(t)$, where $k_{\max} = N/2$ denotes the Nyquist wavenumber and $\eta(t) = (\nu^3/\varepsilon(t))^{1/4}$ is computed from the spectral dissipation rate $\varepsilon(t) = 2\nu \sum_k k^2 E(k, t)$. Figure 6 shows a representative case from the ensemble (seed = 1009224320). As expected for decaying turbulence, $k_{\max}\eta(t)$ reaches its minimum near the dissipation peak and then increases as the flow decays. Across all $N_s = 1000$ runs, $\min_t(k_{\max}\eta)$ is tightly distributed in [2.165, 2.194] with median 2.180 (IQR [2.177, 2.183]), and the minimum is attained at t_ε in every run. Using the 2/3 de-aliased cutoff $k_{\text{cut}} = N/3$, the corresponding minimum satisfies $\min_t(k_{\text{cut}}\eta) \in [1.443, 1.463]$ (median 1.453), consistent with $k_{\text{cut}}\eta = (2/3)k_{\max}\eta$.

Appendix B: Spectral interpretation of the discrete K_{\max} branches

To clarify how the discrete values of K_{\max} arise and how they relate to the regime dependence reported in Fig. 2, Fig. 10 visualizes the time evolution of the spectra for three representative realizations with $K_{\max} = 33, 34, \text{ and } 36$. Here $C(k, t)$ denotes the isotropic curl-of-vorticity spectrum (proportional to $k^4 E(k, t)$ for incompressible flow), and $k_{\text{peak}}(t) = \arg \max_k C(k, t)$ is shown by red markers. The vertical dotted line indicates the run-wise maximum $K_{\max} = \max_t k_{\text{peak}}(t)$.

Across all three cases, the red markers demonstrate that $k_{\text{peak}}(t)$ intermittently approaches K_{\max} and later departs from it, implying that the maximum-wavenumber state is visited repeatedly rather than at a single instant. The superposed black curves in the zoomed panels show $C(k, t)$ evaluated at the extracted event times $t_{k,\text{first}}$ and $t_{k,\text{last}}$ (first and last hitting times of K_{\max}), together with t_ε and t_M . As expected from the

operational definitions, the spectra at $t_{k,\text{first}}$ and $t_{k,\text{last}}$ attain their maxima at $k = K_{\text{max}}$; the purpose of this overlay is to provide a direct visual sanity check of the extraction procedure and to prevent confusion between K_{max} and other peak-related quantities.

Importantly, K_{max} should not be conflated with the wavenumber at which the global amplitude maximum occurs. The maximum spectral amplitude is $M_{\text{max}} = \max_t \max_k C(k, t)$ at time t_M , and its associated peak location is $k_{\text{peak}}(t_M)$, which need not coincide with K_{max} (e.g., in the representative $K_{\text{max}} = 34$ case, $k_{\text{peak}}(t_M) = 31$). Comparing the three realizations, the $K_{\text{max}} = 36$ case exhibits a noticeable bias of the curvature-weighted activity toward smaller scales: the peak location at the maximum-amplitude time is shifted to a higher wavenumber ($k_{\text{peak}}(t_M) = 34$) compared with the dominant $K_{\text{max}} = 34$ case. This trend is consistent with the conditional statistics in Fig. 2, where the high- K_{max} branch shows a substantially elevated probability of lagging precursor times ($\Delta t_{\varepsilon, k} < 0$), suggesting that realizations that access a higher- K_{max} pathway are more prone to delayed migration of $k_{\text{peak}}(t)$ relative to the dissipation peak.

Appendix C: Pickands–Balkema–de Haan theorem and generalized Pareto distributions

The following appendix provides a self-contained discussion of the theoretical basis for the POT method used in Sec. III.

Conditional excess distributions.

Let X be a real-valued random variable with distribution function $F(x) = \Pr(X \leq x)$ and survival function $\bar{F}(x) = 1 - F(x)$. Let the (right) endpoint be

$$x_F := \sup\{x \in \mathbb{R} : F(x) < 1\} \in (-\infty, \infty]. \quad (\text{C1})$$

In the main text, we denote by x_{end} the finite upper endpoint implied by the fitted GPD under $\xi < 0$. In the asymptotic limit $u \rightarrow x_F$, this estimator approximates the theoretical right endpoint x_F .

Fix a threshold $u < x_F$ such that $\bar{F}(u) > 0$. The (*conditional*) *excess distribution* above u is defined for $y \geq 0$ (with $u + y < x_F$) by

$$F_u(y) := \Pr(X - u \leq y \mid X > u). \quad (\text{C2})$$

By the definition of conditional probability,

$$F_u(y) = \frac{\Pr(u < X \leq u + y)}{\Pr(X > u)} = \frac{F(u + y) - F(u)}{\bar{F}(u)}. \quad (\text{C3})$$

Equivalently, the conditional survival function of the ex-

ceedance is the *tail ratio*

$$\begin{aligned} \bar{F}_u(y) &:= 1 - F_u(y) \\ &= \Pr(X - u > y \mid X > u) \\ &= \frac{\Pr(X > u + y)}{\Pr(X > u)} \\ &= \frac{\bar{F}(u + y)}{\bar{F}(u)}. \end{aligned} \quad (\text{C4})$$

The PBdH theorem characterizes when $\bar{F}_u(\cdot)$ has an approximately universal form for *high* thresholds u .

Generalized Pareto distribution and POT

The generalized Pareto distribution (GPD) with shape parameter $\xi \in \mathbb{R}$ and scale $\beta > 0$ has distribution function

$$H_{\xi, \beta}(y) = \begin{cases} 1 - (1 + \xi y / \beta)^{-1/\xi}, & \xi \neq 0, \\ 1 - \exp(-y/\beta), & \xi = 0, \end{cases} \quad (\text{C5})$$

defined for $y \geq 0$ subject to $1 + \xi y / \beta > 0$ (so that for $\xi < 0$ the support is $0 \leq y \leq -\beta/\xi$). A key property is *threshold stability*: if $Y \sim \text{GPD}(\xi, \beta)$ and $t > 0$ is such that $\Pr(Y > t) > 0$, then

$$(Y - t \mid Y > t) \sim \text{GPD}(\xi, \beta + \xi t), \quad (\text{C6})$$

i.e., the shape ξ is invariant under further thresholding while the scale updates linearly [18, 19]. In POT modeling, one chooses a high threshold u and models the excess $Y = X - u$ conditional on $X > u$ as GPD. The mathematical justification is provided by the PBdH theorem [5, 6].

Pickands–Balkema–de Haan theorem

There are several equivalent formulations; we state a standard version emphasizing uniform convergence of the excess distribution.

Assume throughout this section that $(X_i)_{i \geq 1}$ are independent and identically distributed (i.i.d.) copies of X , and define the sample maximum $M_n = \max\{X_1, \dots, X_n\}$. The distribution F is said to belong to the maximum domain of attraction of the generalized extreme-value (GEV) distribution with index ξ if there exist normalizing sequences $a_n > 0$ and $b_n \in \mathbb{R}$ such that

$$\Pr\left(\frac{M_n - b_n}{a_n} \leq z\right) \rightarrow G_\xi(z), \quad n \rightarrow \infty, \quad (\text{C7})$$

where the GEV cdf is

$$G_\xi(z) = \begin{cases} \exp(-(1 + \xi z)^{-1/\xi}), & \xi \neq 0, \\ \exp(-e^{-z}), & \xi = 0, \end{cases} \quad (\text{C8})$$

with support restricted to $1 + \xi z > 0$ when $\xi \neq 0$ [20, 21]. Under this assumption, high-threshold exceedances admit a GPD approximation [5, 6].

Assume that X has distribution function F in the *maximum domain of attraction* of a GEV distribution with extreme-value index ξ , denoted $F \in \text{MDA}(\text{GEV}_\xi)$ [20, 21]. Then there exists a positive function $\beta(u)$ such that, as $u \rightarrow x_F$,

$$\sup_{0 \leq y < x_F - u} |F_u(y) - H_{\xi, \beta(u)}(y)| \rightarrow 0, \quad (\text{C9})$$

where $H_{\xi, \beta}$ is the GPD cdf in Eq. (C5). Conversely, if the excess distributions satisfy Eq. (C9) for some ξ and some positive $\beta(u)$, then $F \in \text{MDA}(\text{GEV}_\xi)$; thus the GPD limit for exceedances and the GEV limit for maxima are two sides of the same asymptotic regularity [20, 21]. In words, for sufficiently high thresholds, the conditional excess distribution is well approximated by a GPD whose shape parameter ξ matches the GEV extreme-value index, while the scale $\beta(u)$ may depend on the threshold. The case $\xi > 0$ corresponds to heavy-tailed (Fréchet-type) behavior; $\xi = 0$ to Gumbel-type; and $\xi < 0$ to finite-endpoint (Weibull-type) behavior [18, 20].

Derivation sketch via tail quantiles and extended regular variation

This section sketches how the GPD form emerges from the tail ratio in Eq. (C4) under the MDA assumption. A convenient tool is the *tail quantile function*

$$U(t) := F^{\leftarrow} \left(1 - \frac{1}{t} \right), \quad t > 1, \quad (\text{C10})$$

where F^{\leftarrow} is the generalized inverse (so that the definition remains valid even if F is not strictly invertible) [20]. By construction, $\Pr(X > U(t)) = 1/t$.

Extended regular variation

A cornerstone equivalence in extreme-value theory is that

$$F \in \text{MDA}(\text{GEV}_\xi) \iff U \in \text{ERV}_\xi, \quad (\text{C11})$$

where ERV_ξ denotes *extended regular variation* with index ξ [20–22]. Concretely, $U \in \text{ERV}_\xi$ means that there exists a scaling function $a(t) > 0$ such that for each fixed $x > 0$,

$$\frac{U(tx) - U(t)}{a(t)} \rightarrow \begin{cases} \frac{x^\xi - 1}{\xi}, & \xi \neq 0, \\ \log x, & \xi = 0, \end{cases} \quad (t \rightarrow \infty). \quad (\text{C12})$$

For the purposes of this note, Eq. (C12) can be taken as a standard characterization of the MDA condition [20].

From ERV to the GPD tail ratio

Choose a high threshold of the form

$$u = U(t), \quad t \rightarrow \infty. \quad (\text{C13})$$

Consider normalized exceedances $(X - u)/a(t)$ conditional on $X > u$. Using Eq. (C4), for $y \geq 0$ we have

$$\Pr \left(\frac{X - u}{a(t)} > y \mid X > u \right) = \frac{\Pr(X > u + a(t)y)}{\Pr(X > u)}. \quad (\text{C14})$$

Case $\xi \neq 0$. Fix $y \geq 0$ and set

$$x = (1 + \xi y)^{1/\xi}, \quad \text{equivalently} \quad y = \frac{x^\xi - 1}{\xi}. \quad (\text{C15})$$

By ERV in Eq. (C12), $U(tx) \approx U(t) + a(t)y$, i.e.,

$$u + a(t)y \approx U(tx). \quad (\text{C16})$$

Using $\Pr(X > U(t)) = 1/t$ and $\Pr(X > U(tx)) = 1/(tx)$,

$$\frac{\Pr(X > u + a(t)y)}{\Pr(X > u)} \approx \frac{\Pr(X > U(tx))}{\Pr(X > U(t))} = \frac{1/(tx)}{1/t} = \frac{1}{x}. \quad (\text{C17})$$

Substituting Eq. (C15) yields

$$\Pr \left(\frac{X - u}{a(t)} > y \mid X > u \right) \rightarrow (1 + \xi y)^{-1/\xi}, \quad (t \rightarrow \infty). \quad (\text{C18})$$

Taking complements, the corresponding conditional cdf converges to

$$\Pr \left(\frac{X - u}{a(t)} \leq y \mid X > u \right) \rightarrow 1 - (1 + \xi y)^{-1/\xi}, \quad (\text{C19})$$

which is the GPD with unit scale in Eq. (C5).

Case $\xi = 0$. ERV gives $(U(tx) - U(t))/a(t) \rightarrow \log x$. Choose $x = e^y$ so that $\log x = y$. Proceeding as above yields

$$\Pr \left(\frac{X - u}{a(t)} > y \mid X > u \right) \rightarrow e^{-y}, \quad (\text{C20})$$

i.e., the exponential limit corresponding to the $\xi = 0$ GPD.

Returning to unnormalized excesses

The limits above are for the *scaled* exceedance $(X - u)/a(t)$ with $u = U(t)$. Equivalently, defining $\beta(u) := a(t)$ when $u = U(t)$, we may rewrite the approximation in the original scale as

$$\Pr(X - u \leq y \mid X > u) \approx H_{\xi, \beta(u)}(y) = 1 - \left(1 + \xi \frac{y}{\beta(u)} \right)^{-1/\xi}, \quad (\text{C21})$$

with the exponential form for $\xi = 0$. This is the content of Eq. (C9), and it explains why the GPD emerges as the universal limit for high-threshold exceedances.

Worked example: Pareto

For the Pareto (Type I) distribution with parameters $x_m > 0$ and $\alpha > 0$,

$$F(x) = 1 - \left(\frac{x_m}{x}\right)^\alpha, \quad x \geq x_m, \quad (\text{C22})$$

the survival function is $\bar{F}(x) = (x_m/x)^\alpha$. The tail quantile is explicit:

$$U(t) = F^{-1}\left(1 - \frac{1}{t}\right) = x_m t^{1/\alpha}. \quad (\text{C23})$$

Setting $\xi = 1/\alpha$ and $a(t) = (x_m/\alpha)t^{1/\alpha}$, one finds

$$\frac{U(tx) - U(t)}{a(t)} = \frac{x^\xi - 1}{\xi} \quad (\text{C24})$$

exactly (no limiting argument needed), hence $F \in \text{MDA}(\text{GEV}_\xi)$.

Moreover, the excess distribution above any threshold $u \geq x_m$ is *exactly* GPD: using Eq. (C4),

$$\bar{F}_u(y) = \frac{\bar{F}(u+y)}{\bar{F}(u)} = \left(\frac{u}{u+y}\right)^\alpha = \left(1 + \frac{y}{u}\right)^{-\alpha}. \quad (\text{C25})$$

Comparing with the GPD survival function $(1 + \xi y/\beta)^{-1/\xi}$ shows that

$$X - u \mid X > u \sim \text{GPD}\left(\xi = \frac{1}{\alpha}, \beta = \frac{u}{\alpha}\right). \quad (\text{C26})$$

Thus the PBdH approximation becomes an identity for Pareto tails.

Practical remarks for applications.

The PBdH theorem is asymptotic in the threshold: $u \rightarrow x_F$ (or $u \rightarrow \infty$ if $x_F = \infty$). In finite samples, one typically chooses a high threshold $u = u_n$ such that the number of exceedances k_n satisfies $k_n \rightarrow \infty$ while $k_n/n \rightarrow 0$ as $n \rightarrow \infty$ (an *intermediate* sequence), balancing bias and variance [18, 20]. When observations are dependent (e.g., time series), exceedances may cluster; declustering or extremal-index corrections are commonly used in POT practice [18, 19].

In conclusion, starting from the conditional excess distribution in Eq. (C2), the tail-ratio identity in Eq. (C4) reduces the problem to understanding $\bar{F}(u+y)/\bar{F}(u)$ for

large u . Under the MDA/ERV regularity condition, the scaled exceedance tail converges to the GPD form, yielding the PBdH theorem and providing the mathematical basis for POT modeling of extremes.

Appendix D: POT threshold and uncertainty diagnostics

To address potential sensitivity to the threshold choice u and to quantify uncertainty in the generalized Pareto (GPD) tail parameters, we carried out complementary diagnostic checks. First, as u is increased, the number of exceedances n_u must decrease by construction; the resulting threshold–sample-size tradeoff is shown explicitly in Fig. 7(e–h). Second, we assess finite-sample uncertainty by fixed-threshold bootstrap resampling ($B = 2000$), summarized in Table III. Here, “finite endpoint” statistics are computed only over bootstrap replicates with $\hat{\xi} < 0$, while p_∞ denotes the bootstrap frequency of $\hat{\xi} \geq 0$ (unbounded endpoint).

In addition to the endpoint resampling shown in Fig. 7, we also inspect the bootstrap variability of the GPD parameters themselves. Figure 8 displays the fixed-threshold bootstrap distributions ($B = 2000$) of the fitted shape $\hat{\xi}$ and scale $\hat{\beta}$ (dashed lines: original-sample MLEs). Even when the implied endpoint estimate is relatively concentrated, the marginal histograms of $(\hat{\xi}, \hat{\beta})$ can be noticeably asymmetric and may occasionally exhibit secondary structure. This behavior is consistent with the strong finite-sample dependence between ξ and β in POT inference and with the fact that the endpoint $x_{\text{end}} = u - \beta/\xi$ (for $\xi < 0$) is a nonlinear combination of the two parameters; different (ξ, β) pairs can therefore yield comparable endpoint values. Importantly, the bootstrap mass remains overwhelmingly in the $\hat{\xi} < 0$ regime (see also the small unbounded-endpoint frequency p_∞ in Table III), supporting the bounded-tail interpretation at the adopted threshold.

As a complementary threshold diagnostic, Fig. 9 shows mean residual life (MRL) curves, i.e. the empirical mean excess $e(u) = \mathbb{E}[X - u \mid X > u]$ plotted against the threshold u with ± 1 standard-error bars. For a GPD tail, $e(u)$ is approximately affine in u ; in particular, when $\xi < 0$ it is expected to decrease roughly linearly as u approaches the finite endpoint. The present MRL plots are broadly consistent with this expectation over intermediate thresholds, whereas they become progressively noisier at the highest thresholds because the number of exceedances n_u rapidly decreases (cf. Fig. 7(e–h)). Taken together, Figs. 7–9 provide a qualitative validation of the chosen POT threshold and a transparent view of the finite-sample uncertainty in the inferred tail parameters.

[1] S. Tsuzuki, Spectrum of the curl of vorticity as a precursor to dissipation in three-dimensional Taylor-Green

turbulence, Phys. Rev. Fluids **11**, L012601 (2026).

TABLE III. Bootstrap uncertainty summary for fixed-threshold POT fits ($B = 2000$). Here “finite endpoint” statistics are computed only over bootstrap replicates with $\hat{\xi} < 0$. The fraction p_∞ denotes the bootstrap frequency of $\hat{\xi} \geq 0$ (unbounded endpoint). For each variable, the reported $\hat{\xi}$, $\hat{\beta}$, and \hat{x}_{end} are maximum-likelihood estimates (MLEs), with 95% confidence intervals given in brackets.

| Variable | $\hat{\xi}$ (95% CI) | $\hat{\beta}$ (95% CI) | \hat{x}_{end} (95% CI) | p_∞ |
|--|-------------------------|------------------------|---------------------------------|------------|
| $-\Delta t_{\varepsilon,k}^{(\text{first})}$ | -0.228 [-0.451, -0.097] | 0.421 [0.332, 0.557] | 2.097 [1.375, 3.886] | 0.002 |
| $-\Delta t_{\varepsilon,k}^{(s=0.95)}$ | -0.239 [-0.424, -0.110] | 0.431 [0.336, 0.578] | 1.803 [1.183, 3.316] | 0.001 |
| $-\Delta t_{\varepsilon,k}^{(\text{last})}$ | -0.226 [-0.423, -0.086] | 0.310 [0.241, 0.403] | 2.718 [2.237, 4.264] | 0.000 |
| M_{max} | -0.256 [-0.622, -0.125] | 0.953 [0.769, 1.363] | 79.764 [78.039, 82.468] | 0.000 |

- [2] S. Tsuzuki, A curvature-weighted spectral precursor to dissipation in decaying three-dimensional turbulence: robustness across initial conditions and viscosity effects (2026), arXiv:2601.14043 [physics.flu-dyn].
- [3] R. A. Fisher and L. H. C. Tippett, Limiting forms of the frequency distribution of the largest or smallest member of a sample, *Mathematical Proceedings of the Cambridge Philosophical Society* **24**, 180 (1928).
- [4] B. Gnedenko, Sur la distribution limite du terme maximum d’une série aléatoire, *Annals of Mathematics* **44**, 423 (1943).
- [5] J. Pickands, Statistical inference using extreme order statistics, *The Annals of Statistics* **3**, 119 (1975).
- [6] A. A. Balkema and L. de Haan, Residual life time at great age, *The Annals of Probability* **2**, 792 (1974).
- [7] N. Goldenfeld, N. Guttenberg, and G. Gioia, Extreme fluctuations and the finite lifetime of the turbulent state, *Physical Review E* **81**, 035304 (2010).
- [8] D. Faranda, V. Lucarini, P. Manneville, and J. Wouters, On using extreme values to detect global stability thresholds in multi-stable systems: The case of transitional plane Couette flow, *Chaos, Solitons & Fractals* **64**, 26 (2014).
- [9] T. Nemoto and A. Alexakis, Do extreme events trigger turbulence decay? – a numerical study of turbulence decay time in pipe flows, *Journal of Fluid Mechanics* **912**, A38 (2021).
- [10] S. Gomé, L. S. Tuckerman, and D. Barkley, Extreme events in transitional turbulence, *Philosophical Transactions of the Royal Society A: Mathematical, Physical and Engineering Sciences* **380**, 20210036 (2022).
- [11] P. K. Yeung, X. M. Zhai, and K. R. Sreenivasan, Extreme events in computational turbulence, *Proceedings of the National Academy of Sciences of the United States of America* **112**, 12633 (2015).
- [12] E.-W. Saw, D. Kuzzay, D. Faranda, A. Guittonneau, F. Daviaud, C. Wiertel-Gasquet, V. Padilla, and B. Dubrulle, Experimental characterization of extreme events of inertial dissipation in a turbulent swirling flow, *Nature Communications* **7**, 12466 (2016).
- [13] D. Buaria, A. Pumir, E. Bodenschatz, and P.-K. Yeung, Extreme velocity gradients in turbulent flows, *New Journal of Physics* **21**, 043004 (2019).
- [14] D. Buaria, A. Pumir, and E. Bodenschatz, Self-attenuation of extreme events in Navier–Stokes turbulence, *Nature Communications* **11**, 5852 (2020).
- [15] M. Farazmand and T. P. Sapsis, A variational approach to probing extreme events in turbulent dynamical systems, *Science Advances* **3**, e1701533 (2017).
- [16] T. P. Sapsis, Statistics of extreme events in fluid flows and waves, *Annual Review of Fluid Mechanics* **53**, 85 (2021).
- [17] G. I. Taylor and A. E. Green, Mechanism of the production of small eddies from large ones, *Proceedings of the Royal Society of London. A. Mathematical and Physical Sciences* **158**, 499 (1937).
- [18] S. Coles, *An Introduction to Statistical Modeling of Extreme Values* (Springer, 2001).
- [19] P. Embrechts, C. Klüppelberg, and T. Mikosch, *Modelling Extremal Events: for Insurance and Finance* (Springer, 1997).
- [20] L. de Haan and A. Ferreira, *Extreme Value Theory: An Introduction* (Springer, 2006).
- [21] S. I. Resnick, *Extreme Values, Regular Variation and Point Processes* (Springer, 1987).
- [22] N. H. Bingham, C. M. Goldie, and J. L. Teugels, *Regular Variation* (Cambridge University Press, 1987).

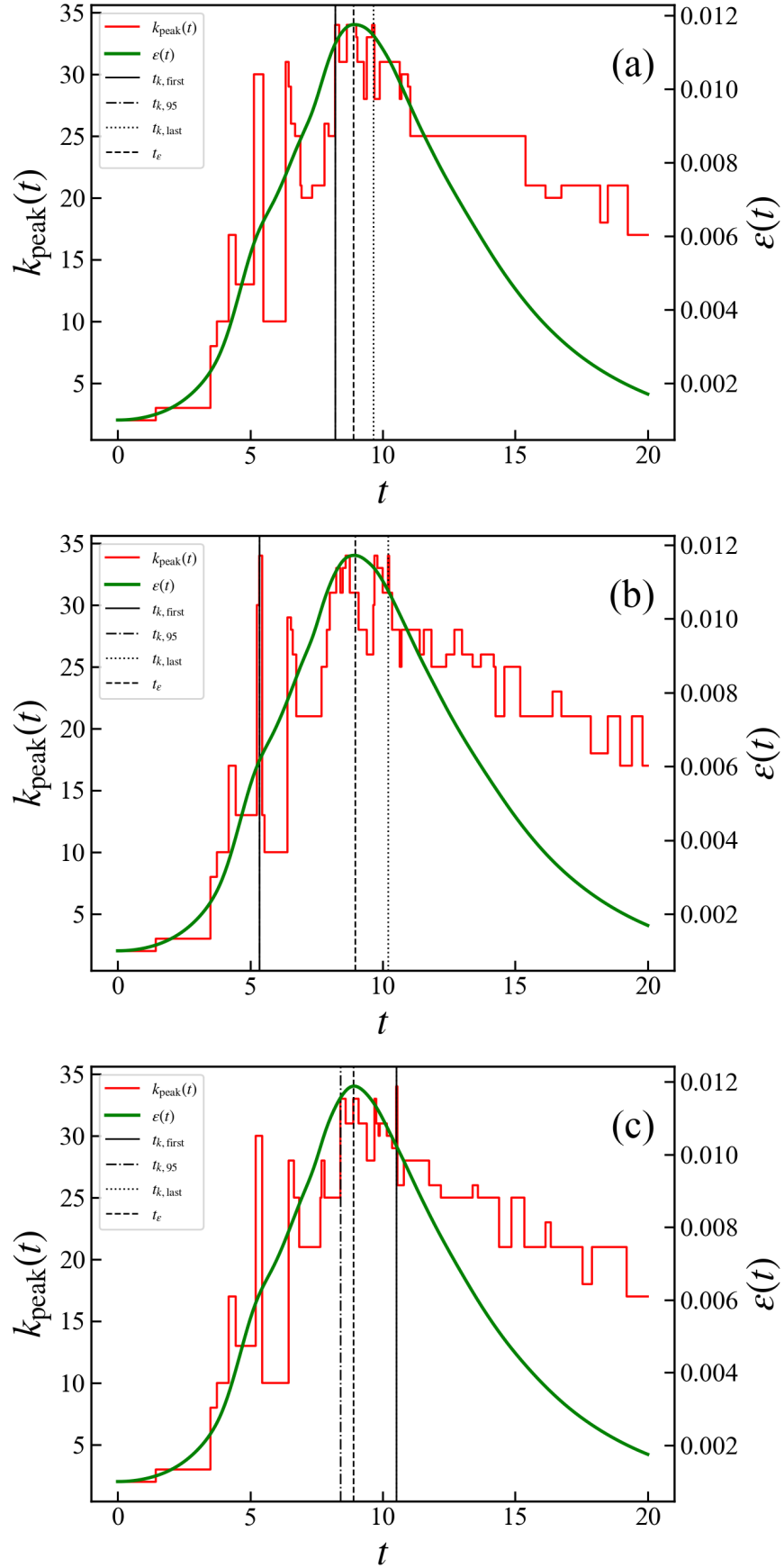


FIG. 1. Example time series of the spectral peak wavenumber $k_{\text{peak}}(t)$ (red) and viscous dissipation rate $\varepsilon(t)$ (green), illustrating typical, leading, and lagging realizations. Vertical lines indicate the timing markers $t_{k, \text{first}}$, $t_{k, 95}$, $t_{k, \text{last}}$, and t_ε .

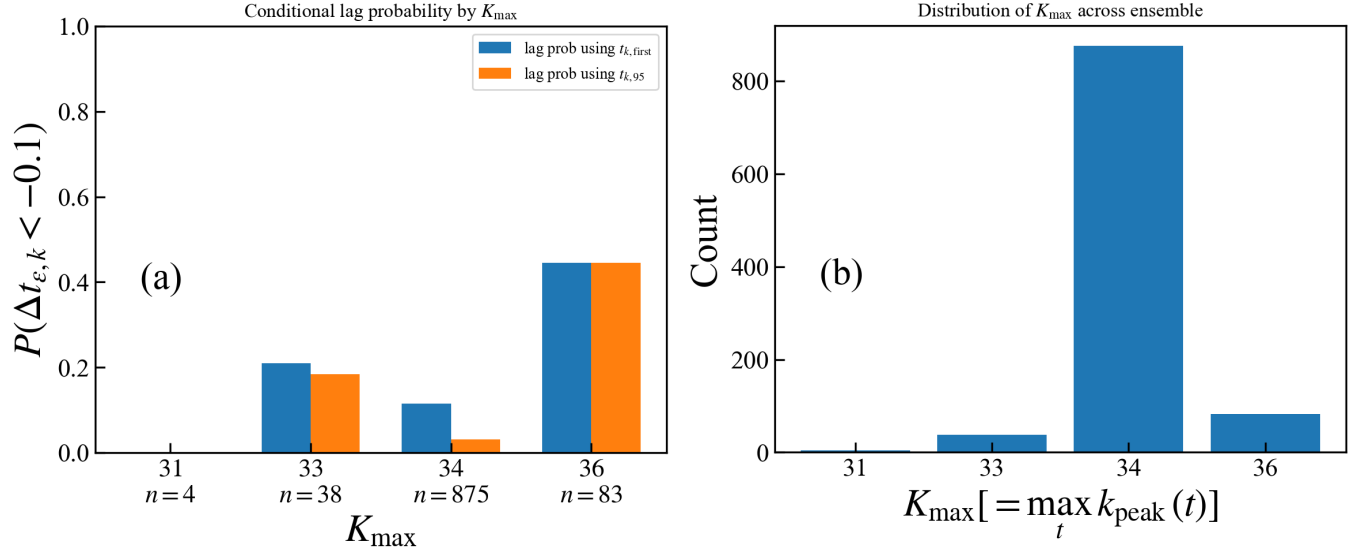


FIG. 2. (a) Conditional lag probability $\Pr(\Delta t_{\varepsilon, k} < -0.1)$ as a function of K_{\max} , comparing $t_{k, \text{first}}$ and $t_{k, 95}$. (b) Histogram of K_{\max} across the $N_s = 1000$ ensemble.

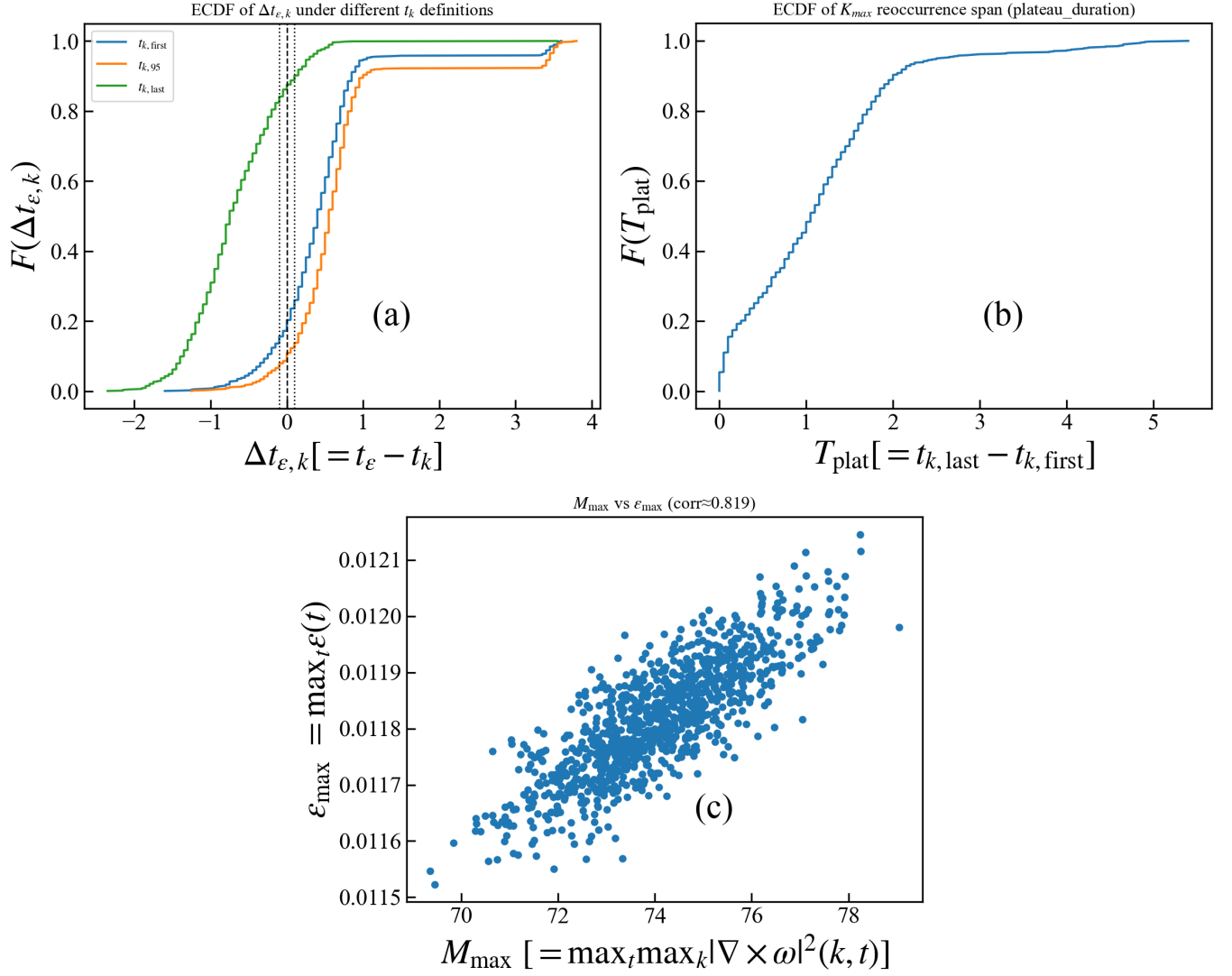


FIG. 3. (a) ECDF of $\Delta t_{\epsilon,k} = t_\epsilon - t_k$ for three t_k definitions. (b) ECDF of the K_{max} plateau duration $T_{\text{plat}} = t_{k, \text{last}} - t_{k, \text{first}}$. (c) Scatter plot of M_{max} versus ϵ_{max} showing a strong correlation across the ensemble.

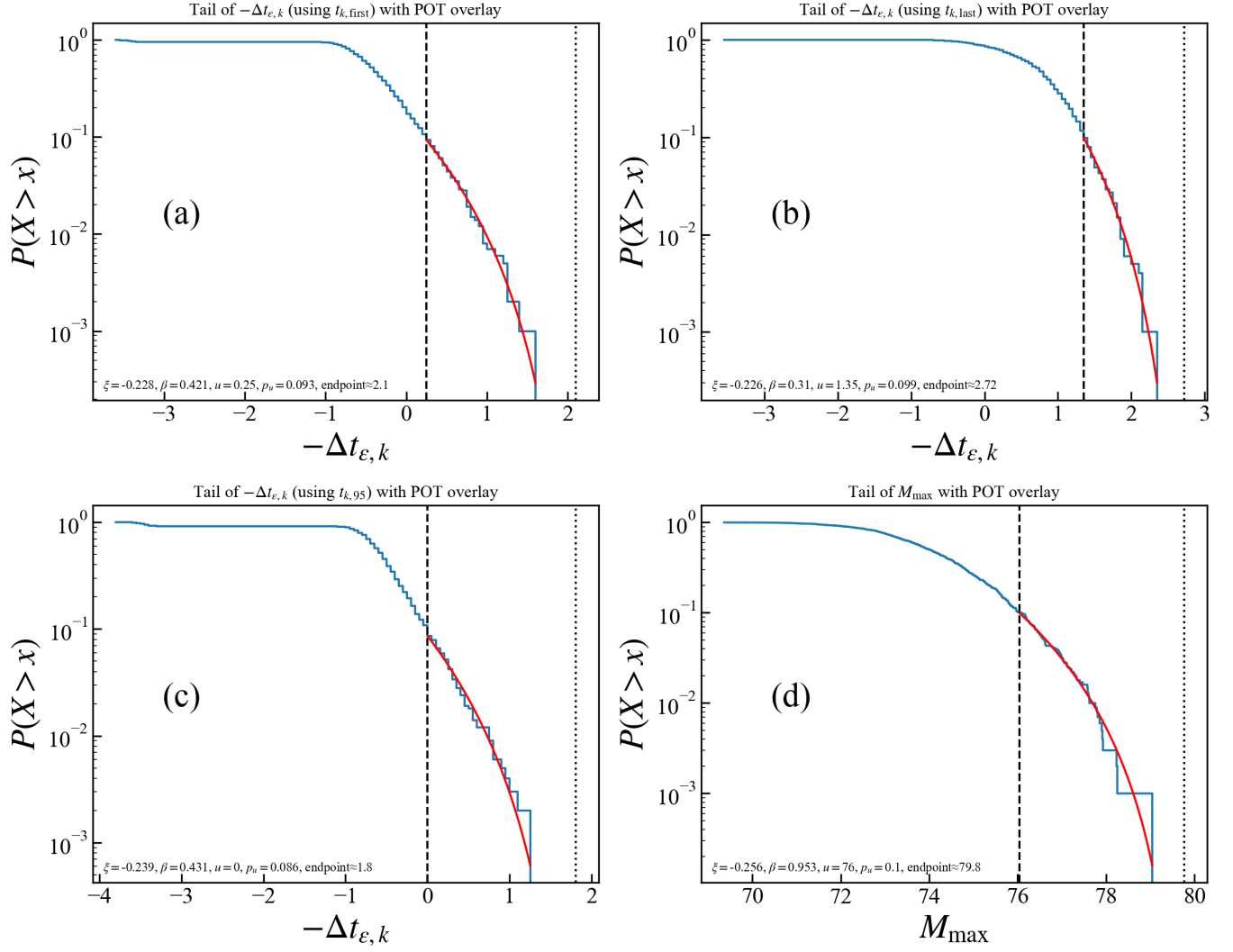


FIG. 4. POT EVT analysis of upper tails. (a)–(c) Tail of the lag magnitude $X = -\Delta t_{\varepsilon, k}$ for different t_k definitions, with GPD fit overlay. (d) Tail of M_{\max} with GPD fit overlay. Dashed vertical lines indicate the threshold u and dotted lines indicate the implied finite endpoint when $\hat{\xi} < 0$.

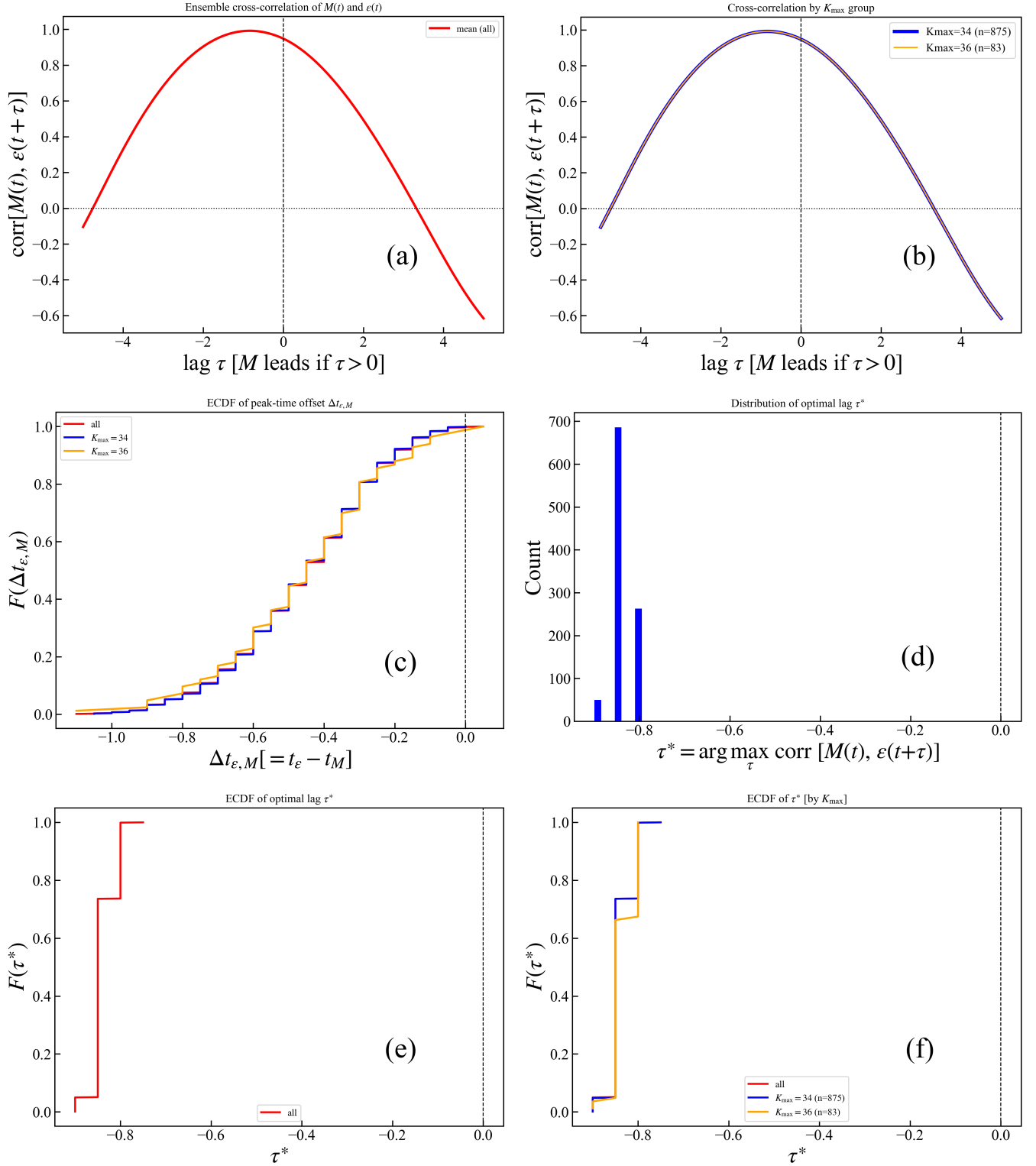


FIG. 5. Time-resolved relationship between the curl-of-vorticity amplitude $M(t)$ and dissipation $\varepsilon(t)$. (a) Ensemble-mean cross-correlation $\text{corr}[M(t), \varepsilon(t + \tau)]$. (b) Cross-correlation by K_{\max} group (dominant groups $K_{\max} = 34$ and 36 shown). (c) ECDF of $\Delta t_{\varepsilon, M} = t_{\varepsilon} - t_M$ (negative indicates M peaks after ε). (d)–(f) Distribution and ECDFs of the optimal lag $\tau^* = \arg \max_{\tau} \text{corr}[M(t), \varepsilon(t + \tau)]$.

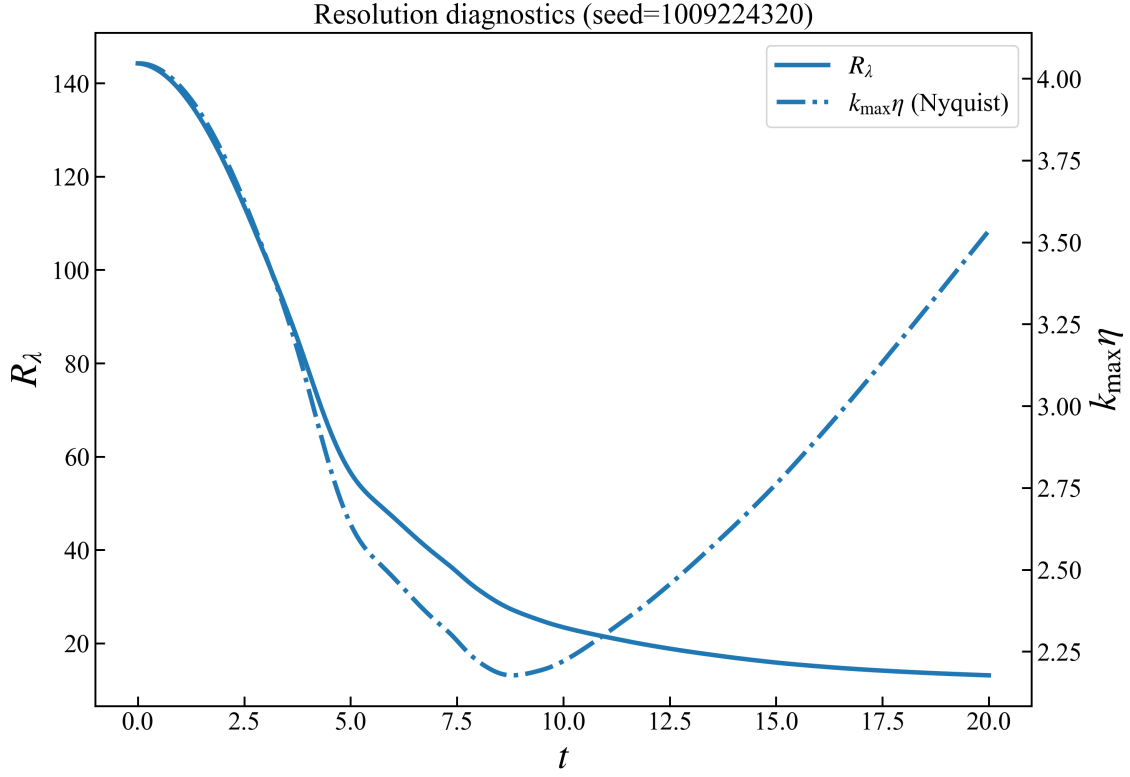


FIG. 6. Representative time series (seed = 1009224320) of the Taylor-microscale Reynolds number $R_\lambda(t)$ (solid line, left axis) and the resolution diagnostic $k_{\max}\eta(t)$ (dash-dotted line, right axis) for the perturbed TGV ensemble at $N = 256^3$ and $\nu = 10^{-3}$. The minimum of $k_{\max}\eta(t)$ occurs near the dissipation peak, where the smallest dissipative scales are expected, and subsequently increases as the flow decays.

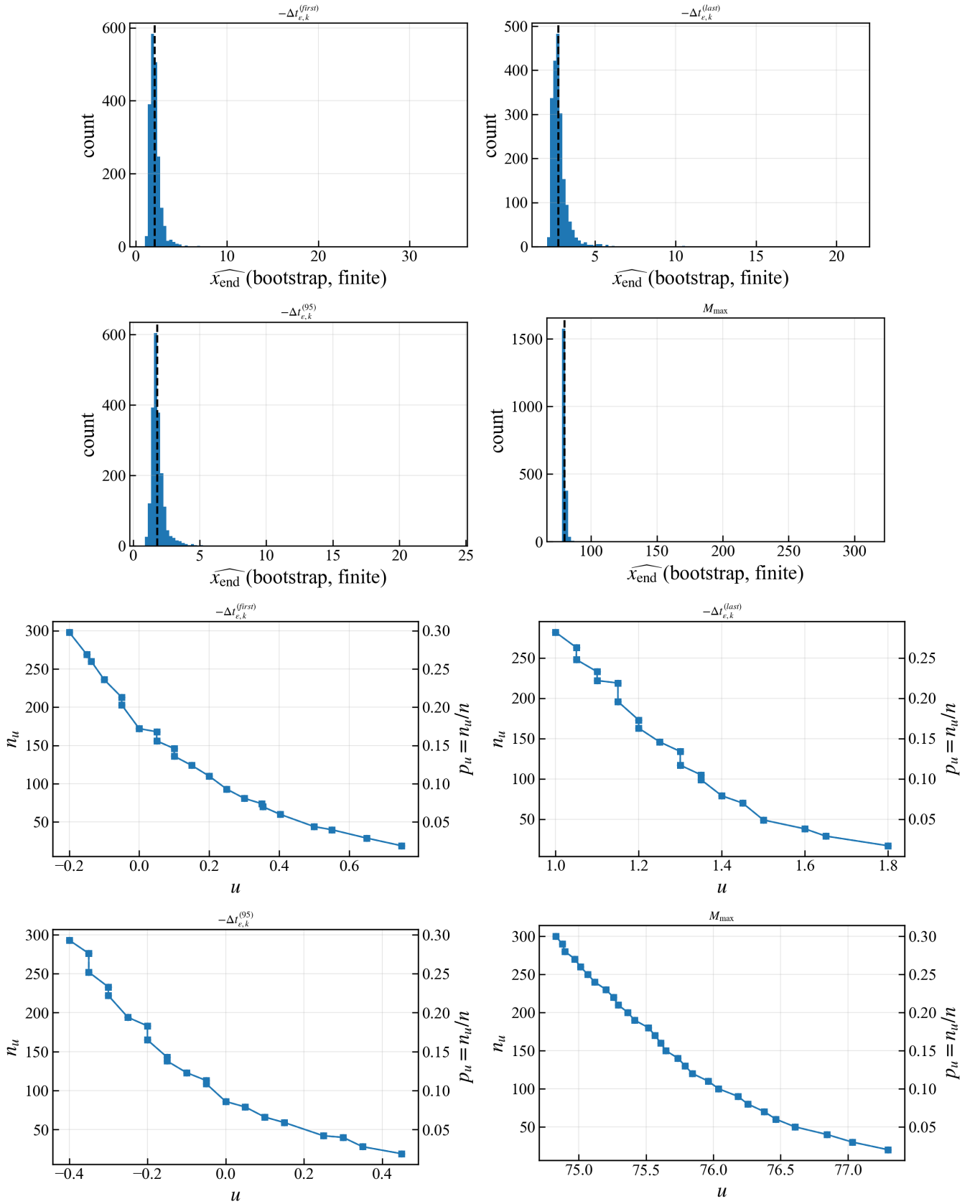


FIG. 7. Bootstrap and threshold tradeoff diagnostics for fixed-threshold POT fits. (a)–(d) Bootstrap histograms of the finite endpoint estimate \hat{x}_{end} (computed only over replicates with $\hat{\xi} < 0$), with the MLE from the original sample overlaid (vertical dashed line). (e)–(h) Exceedance count n_u and exceedance fraction $p_u = n_u/n$ as functions of the threshold u , illustrating the basic tradeoff between tail purity (higher u) and available tail sample size (smaller n_u).

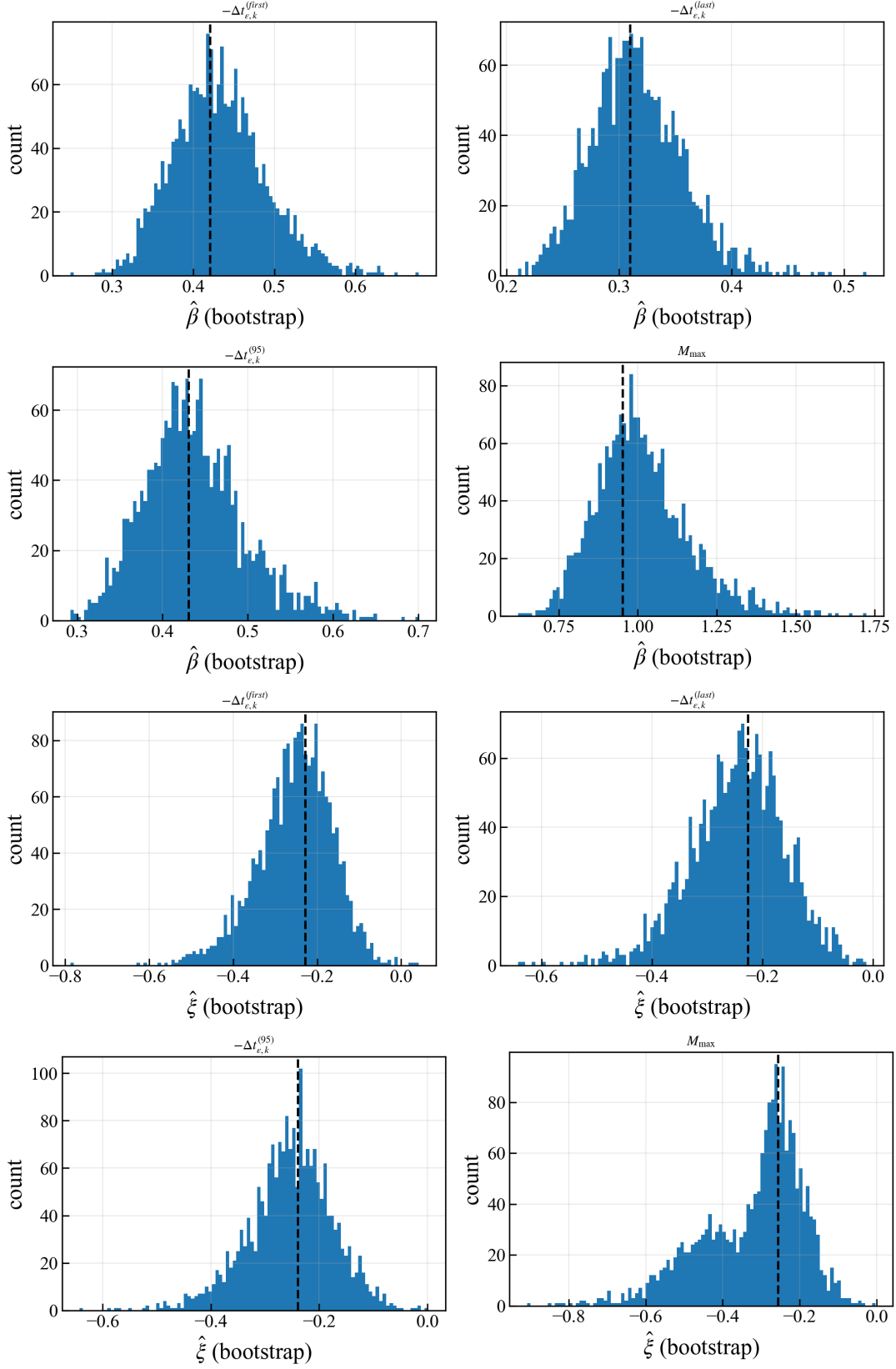


FIG. 8. Bootstrap histograms of the GPD scale $\hat{\beta}$ and shape $\hat{\xi}$ for fixed-threshold POT fits ($B = 2000$). Vertical dashed lines indicate the MLEs from the original sample. While endpoint estimates concentrate tightly (Fig. 7), the parameter histograms can exhibit skewness and occasional secondary modes, reflecting the flexibility of the GPD family and finite-sample sensitivity of (ξ, β) under a bounded-tail constraint.

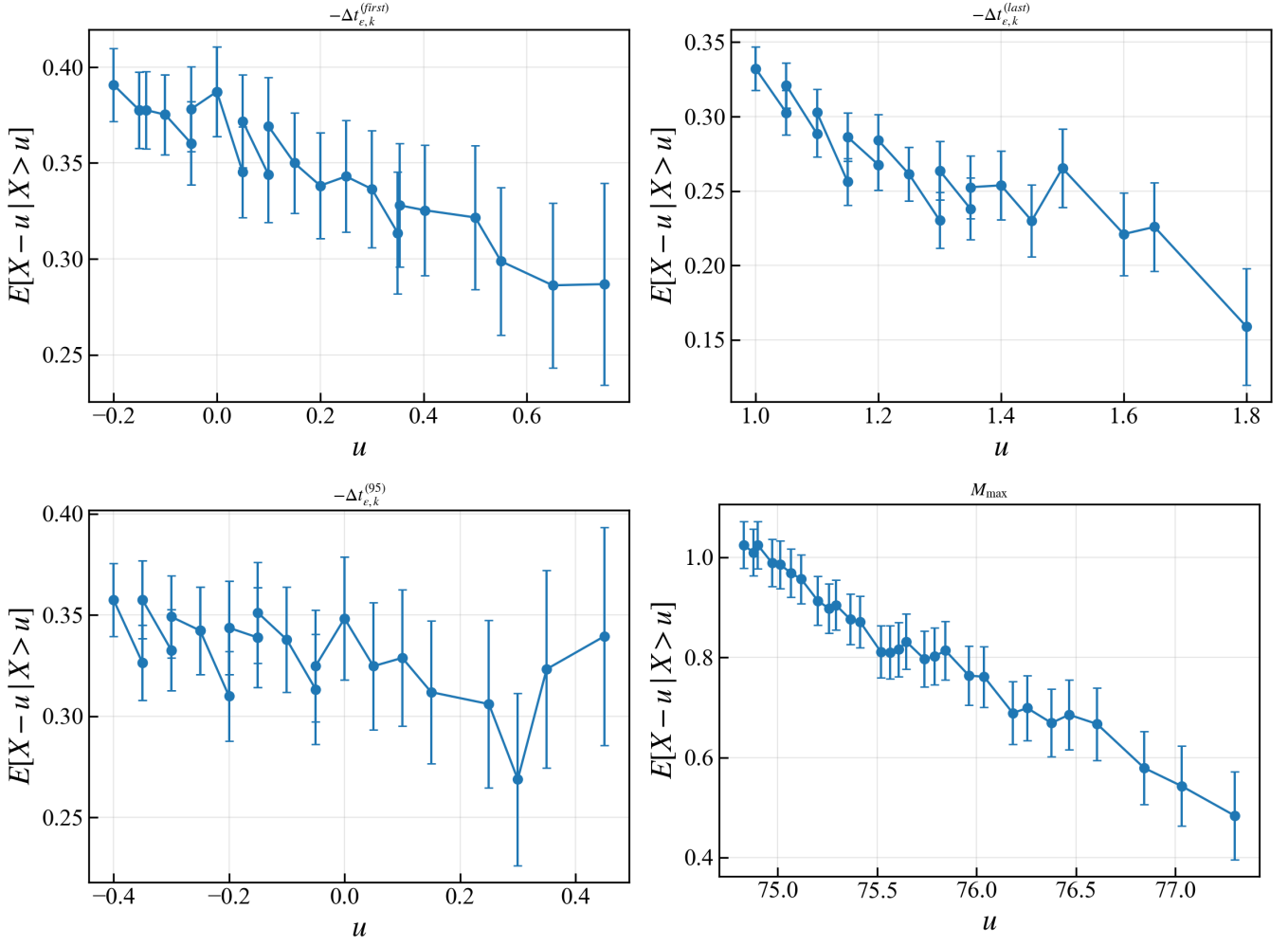


FIG. 9. Mean residual life (MRL) diagnostics, showing $\mathbb{E}[X - u | X > u]$ versus threshold u (with error bars) for each analyzed variable. Error bars indicate ± 1 standard error of the mean excess computed from exceedances above u . For data well described by a GPD above u , the MRL is approximately linear in u ; the present plots provide a qualitative check, but become noisy at high thresholds as n_u decreases.

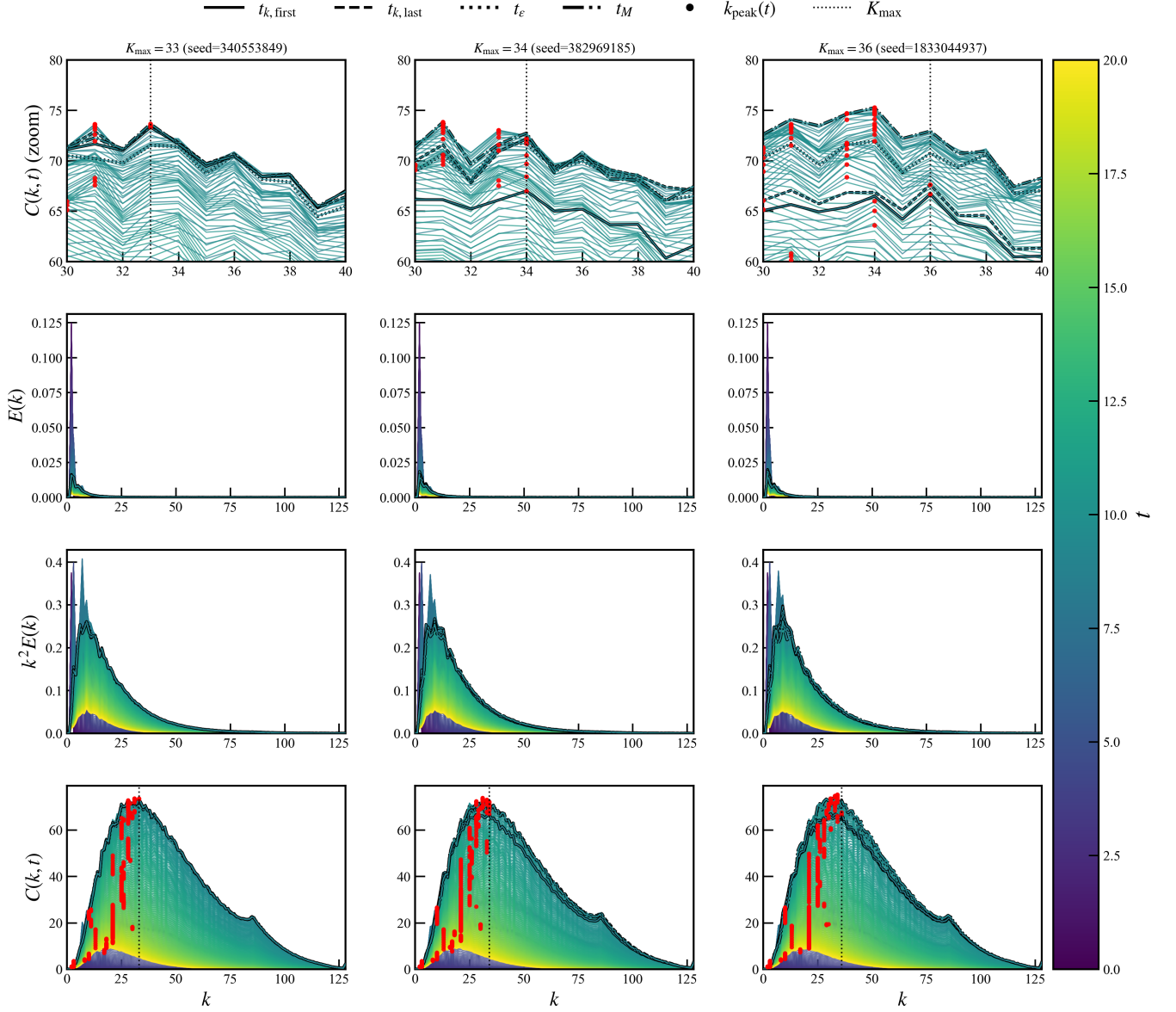


FIG. 10. Spectral evolution for three representative perturbed Taylor–Green vortex (TGV) realizations ($N = 256^3$, $\nu = 10^{-3}$) illustrating the discrete K_{\max} branches. Columns correspond to runs with $K_{\max} = 33, 34,$ and 36 (seeds are given in the panel titles). All panels show shell-averaged spectra colored by time t (shared color bar). The top row shows a zoomed view ($k \in [30, 40]$) of the curl-of-vorticity spectrum $C(k, t)$, defined as the shell-averaged spectrum of $|\nabla \times \boldsymbol{\omega}|^2$. Rows 2–4 show, respectively, $E(k, t)$, $k^2 E(k, t)$, and $C(k, t)$ over the full resolved wavenumber range. Red markers indicate the instantaneous peak wavenumber $k_{\text{peak}}(t) = \arg \max_k C(k, t)$, and the vertical dotted line marks the run-wise maximum $K_{\max} = \max_t k_{\text{peak}}(t)$. Thick black curves highlight spectra at $t_{k, \text{first}}$ (solid), $t_{k, \text{last}}$ (dashed), t_ϵ (dotted), and t_M (dash-dotted), where $M(t) = \max_k C(k, t)$ and $t_M = \arg \max_t M(t)$. Note that $k_{\text{peak}}(t_M)$ does not necessarily coincide with K_{\max} : K_{\max} is the largest peak wavenumber attained over the trajectory.